High-pressure pool boiling and physical insight of engineered surfaces

by

Nanxi Li

B.S., Dalian Maritime University, 2012

AN ABSTRACT OF A DISSERTATION

submitted in partial fulfillment of the requirements for the degree

DOCTOR OF PHILOSOPHY

Department of Mechanical and Nuclear Engineering
College of Engineering

KANSAS STATE UNIVERSITY
Manhattan, Kansas

2017

Abstract

Boiling is a very effective way of heat transfer due to the latent heat of vaporization. Large amount of heat can be removed as bubbles form and leave the heated surface. Boiling heat transfer has lots of applications both in our daily lives and in the industry. The performance of boiling can be described with two important parameters, i.e. the heat transfer coefficient (HTC) and the critical heat flux (CHF). Enhancing the performance of boiling will greatly increase the efficiency of thermal systems, decrease the size of heat exchangers, and improve the safety of thermal facilities. Boiling heat transfer is an extremely complex process. After over a century of research, the mechanism for the HTC and CHF enhancement is still elusive. Previous research has demonstrated that fluid properties, system pressures, surface properties, and heater properties etc. have huge impact on the performance of boiling. Numerous methods, both active and passive, have been developed to enhance boiling heat transfer. In this work, the effect of pressure was investigated on a plain copper substrate from atmospheric pressure to 45 psig. Boiling heat transfer performance enhancement was then investigated on Teflon© coated copper surfaces, and graphene oxide coated copper surfaces under various system pressures. It was found that both HTC and CHF increases with the system pressure on all three types of surfaces. Enhancement of HTC on the Teflon© coated copper surface is contributed by the decrease in wettability. It is also hypothesized that the enhancement in both HTC and CHF on the graphene oxide coated surface is due to pinning from micro and nanostructures in the graphene oxide coating or non-homogeneous wettability. Condensation and freezing experiments were conducted on engineered surfaces in order to further characterize the pinning effect of non-homogeneous wettability and micro/nano structure of the surface.

High-pressure pool boiling and physical insight of engineered surfaces

by

Nanxi Li

B.S., Dalian Maritime University, 2012

A DISSERTATION

submitted in partial fulfillment of the requirements for the degree

DOCTOR OF PHILOSOPHY

Department of Mechanical and Nuclear Engineering
College of Engineering

KANSAS STATE UNIVERSITY
Manhattan, Kansas

2017

Approved by:

Major Professor
Amy Rachel Betz

Copyright

Abstract

Boiling is a very effective way of heat transfer due to the latent heat of vaporization. Large amount of heat can be removed as bubbles form and leave the heated surface. Boiling heat transfer has lots of applications both in our daily lives and in the industry. The performance of boiling can be described with two important parameters, i.e. the heat transfer coefficient (HTC) and the critical heat flux (CHF). Enhancing the performance of boiling will greatly increase the efficiency of thermal systems, decrease the size of heat exchangers, and improve the safety of thermal facilities. Boiling heat transfer is an extremely complex process. After over a century of research, the mechanism for the HTC and CHF enhancement is still elusive. Previous research has demonstrated that fluid properties, system pressures, surface properties, and heater properties etc. have huge impact on the performance of boiling. Numerous methods, both active and passive, have been developed to enhance boiling heat transfer. In this work, the effect of pressure was investigated on a plain copper substrate from atmospheric pressure to 45 psig. Boiling heat transfer performance enhancement was then investigated on Teflon© coated copper surfaces, and graphene oxide coated copper surfaces under various system pressures. It was found that both HTC and CHF increases with the system pressure on all three types of surfaces. Enhancement of HTC on the Teflon© coated copper surface is contributed by the decrease in wettability. It is also hypothesized that the enhancement in both HTC and CHF on the graphene oxide coated surface is due to pinning from micro and nanostructures in the graphene oxide coating or non-homogeneous wettability. Condensation and freezing experiments were conducted on engineered surfaces in order to further characterize the pinning effect of non-homogeneous wettability and micro/nano structure of the surface.

Table of Contents

List of Figures

List of Tables

List of Abbreviations

HTC = Heat Transfer Coefficient (W/cm^{2}K)

CHF = Critical Heat Flux (W/cm^2)

ONB = Onset of Nucleate Boiling

Nomenclature

A = area (m^2)

Dd = bubble departure diameter (m)

Ecap= energy (J/m^2)

f = bubble release frequency (Hz)

g = gravity (N/kg)

k = thermal conductivity (W/mK)

L = thickness of coating (m)

n’ = pore density ($1/m^2$)

na’ = nucleation site density ($1/m^2$)

p = pressure (Pa)

q = heat transfer rate (W)

q’’ = heat flux (W/cm^2)

r = radius (m)

SA = surface energy (J/m^2)

T = temperature (K)

V = volume (m^3)

Δh = latent heat (kJ/kg)

ΔT = superheat (K)

Δx = distance between thermocouples (m)

Greek Letters

θ = contact angle (˚)

ψ = cavity wedge angle (˚)

σ = surface tension (N/m)

δ = boundary layer thickness (m)

ρ = density (kg/m^3)

υ = specific volume (m^3/kg)

Subscripts

B = bubble

c = contact

L= liquid

sat = saturation

V = vapor

w = wall

Acknowledgements

I would like to express the deepest appreciation to my advisor Dr. Amy Betz for her continuous guidance and help for my research. I would also like to express my gratitude to my committee members, Dr. Eckels, Dr. Fenton, Dr. Amama, and Dr. Sayre for their insights. In addition, I would like to thank Dr. Singh for his input to my research. I would also like to acknowledge Eric Wagner for helping me building the experimental facility. In the end, I would also like to thank my family and friends for their constant support in my pursuit of the PhD. Degree.

Dedication

This work is dedicated to my father, Chaomin Li, and my mother, Xiaomei Ye. Without their unconditional support, care, and love, I would never have gone this far both in the academic world and in life.

Chapter 1 - Introduction

1.1 Pool boiling heat transfer

Boiling is a very common heat transfer process that we experience almost every day in our daily lives. Boiling is defined as “a phase change process in which vapor is formed either on a heated surface or in a superheated liquid layer adjacent to the heated surface” [1]. It is an efficient way to transfer a large amount of heat due to the latent heat of vaporization. As vapor bubbles form on the heated surface, a large amount of heat is removed from the surface. Therefore boiling has extensive applications in the industry, such as power generation, chemical processing, HVAC systems, electronic cooling etc [2].

There are two types of boiling, pool boiling and flow boiling. In pool boiling, the fluid over the heated surface is confined in a pool. When the fluid is heated up, all the motion of the liquid is due to natural convection. On the other hand, in flow boiling, fluid flows over the heated surface. As the surfaces heats up, forced convection takes place over the heated surface [1].

A boiling curve is generally used to describe a pool boiling process. Figure 1.1 is a typical qualitative boiling curve showing the entire boiling process. The x-axis of the boiling curve is wall superheat ΔT, which is defined as the temperature difference between the surface and the bulk fluid. The y-axis of the boiling curve is the rate of heat transferred though a unit area on the heated surface, or heat flux (*q''*).

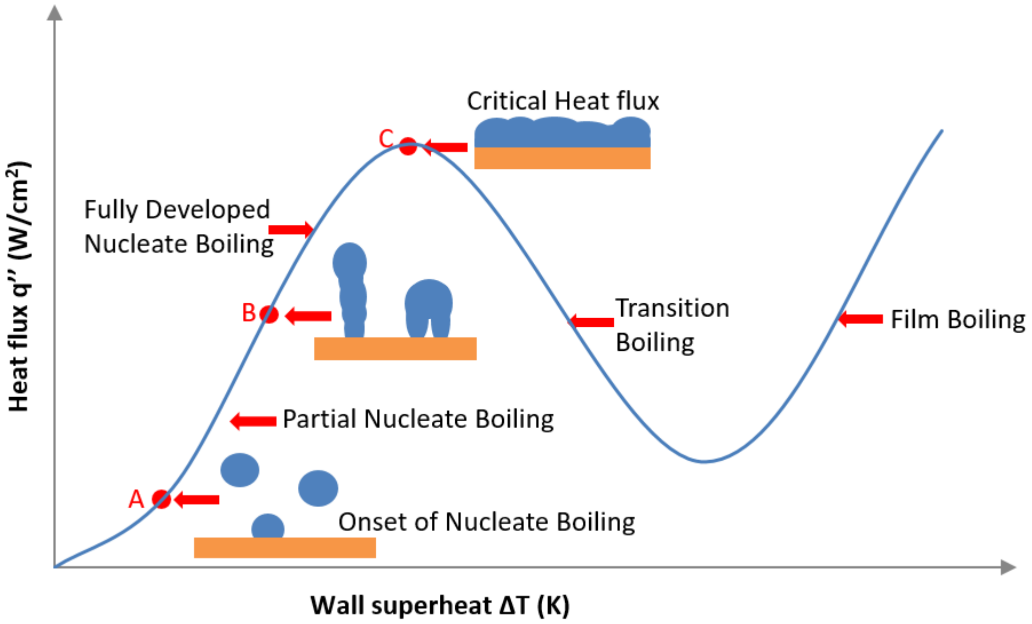

Figure 1.1 A qualitative boiling curve

An entire pool boiling process can be divided in to five boiling regimes, which is shown the in boiling curve. In the first regime, very low heat fluxes are applied to the heated surface, and there is no bubble formation on the surface. Hence natural convection is the only mode of heat transfer in the first regime. As the heat flux applied to the heated surface increase, bubbles will start to form on the surface. The spots where the bubbles form is called a nucleation sites. The formation of the first bubbles is called the onset of nucleation (ONB). This boiling regime where bubbles are formed on discrete sites is defined as the partial nucleate boiling regime. At higher heat fluxes, more and more bubbles form on the surface, and the bubbles are released more frequently. Neighboring bubbles start to merge with each other, and vapor columns are formed in the vertical direction. This boiling regime is called fully developed nucleate boiling. Point C in the boiling curve is the highest heat flux that can be supplied to the heated surface, and the corresponding heat flux is called critical heat flux (CHF). At critical heat flux, all the bubbles forming on the surface are merged with each other, forming a vapor film over the entire surface. The vapor film acts like a thermal barrier for heat transfer, therefore if more heat is applied to the heated surface, the temperature of the surface will rocket uncontrollably causing serious damage to the thermal system [3]. As a result, critical heat flux is a crucial parameter in boiling heat transfer.

If the temperature of the surface is carefully controlled after reaching the critical heat flux, the boiling system will go through transition boiling regime and film boiling regime. However, in this work, only the first three boiling regimes are studied.

Another important parameter in pool boiling is the heat transfer coefficient (HTC). HTC is defined as the ratio of heat flux (q'') and the wall superheat (ΔT). On the boiling curve, HTC is indicated by the slope of the curve. HTC describes how efficient heat is removed from the heated surface during boiling.

1.2 Bubble nucleation

It is reported in the 1950s that bubbles nucleate in small cavities or imperfections on the heated surface 78 [4]. When the contact angle is larger than the cavity wedge angle as shown in Figure 1.2, vapor or gas will be trapped in these cavities and serve as nuclei for bubble nucleation [1].

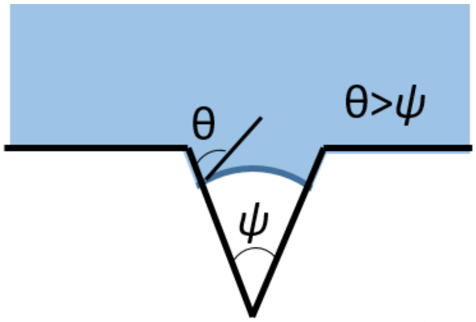

Figure 1.2 Diagram of cavity that can traps vapor/gas

When the bubble is static, a force balance equation can be written at the interface of the bubble and the liquid:

$$p_B - p_L = \frac{2\sigma}{r} \qquad \text{Eq. 1.1}$$

where p_B is the pressure inside the bubble, p_L is the pressure of the liquid, σ is the surface tension, and r is the radius of the bubble.

Since the Gibbs free energy at the phase change line is zero, the pressure difference between the bubble and liquid can be translated to the temperature difference using the Clapeyron equation:

$$\frac{dp}{dT} = \frac{\Delta hp}{\Delta T(\nu_v - \nu_L)} \qquad \text{Eq. 1.2}$$

where Δh is the latent heat of vaporization, $\Delta T = T_w - T_{sat}$, υ_v and υ_L are specific volume of the vapor and liquid respectively. Therefore, for a bubble to grow inside a cavity in saturated boiling conditions when p is much greater than $\frac{2\sigma}{r}$, the minimum temperature difference between the bubble and liquid is written as:

$$T_L - T_{sat} = \frac{2\sigma T_{sat}(\nu_v - \nu_L)}{\Delta hr} \qquad \text{Eq. 1.3}$$

In 1962, Hsu developed a mechanistic model for the size range of the active nucleation cavities [5]. This model assumes that a bubble nucleus will only become a bubble when it is surrounded by superheated liquid, and the heat transfer between the superheated liquid layer and the bubble nucleus is considered to be transient conduction. When the time required for the liquid layer around the nucleus to obtain sufficient superheat for bubble growth is finite, the cavity where the nucleus occurs at is considered to be an active nucleation site. The resulting model is shown in the equation below,

$$\{r_{\max}, r_{\min}\} = \frac{\delta}{2C_1}\left[1 - \frac{\theta_{sat}}{\theta_w} \pm \sqrt{\left(1 - \frac{\theta_{sat}}{\theta_w}\right)^2 - \frac{4AC_3}{\delta\theta_w}}\right] \qquad \text{Eq. 1.4}$$

where $r_{\max}$ and $r_{\min}$ are the maximum and minimum cavity sizes, δ is the boundary layer thickness, $C_1 = (1+\cos\varphi)/\sin\varphi$, $C_3 = (1+\cos\varphi)$, φ is the wetting angle, $A = 2\sigma T_{sat}/\rho_v h_{Lv}$, $\theta_{sat} = T_{sat} - T_f$,and $\theta_w = T_w - T_{sat}$.

In saturated boiling cases, since θ_{sat} is zero, the Eq. 1.5 can be simplified to:

$$\{r_{\max}, r_{\min}\} = \frac{\delta}{2C_1}\left[1 \pm \sqrt{1 - \frac{4AC_3}{\delta\theta_w}}\right] \qquad \text{Eq. 1.5}$$

With this equation, when the boundary layer thickness is known, the range of active nucleation size can be plotted as a function of wall superheat. In saturated boiling case, the boundary layer thickness can be obtained using the following equation:

$$\delta = \sqrt{\frac{4kAC_3}{q_o}} \qquad \text{Eq. 1.6}$$

where k is the thermal conductivity of the fluid, and q_0 is the onset heat flux, which is generally obtained from experimental data.

For example, for the plain copper surface studied in this work, the onset of nucleation occurred at a heat flux of 25 W/cm^2. Contact angle of water on the copper surface was measured to be 68˚. As a result, the boundary layer thickness of bubbles for boiling under atmospheric pressure is calculated to be 25 µm using Eq. 1.6. The size range of active nucleation site range is therefore plotted in Figure 1.3 as a function of wall superheat from 0˚C to 20˚C for both atmospheric pressure and 45 psig. The plot shows pressure has significant effect on the range of active nucleation size. For example, at the same wall super heat of 10 K, the active nucleation size range is much larger at 45 psig than at atmospheric pressure.

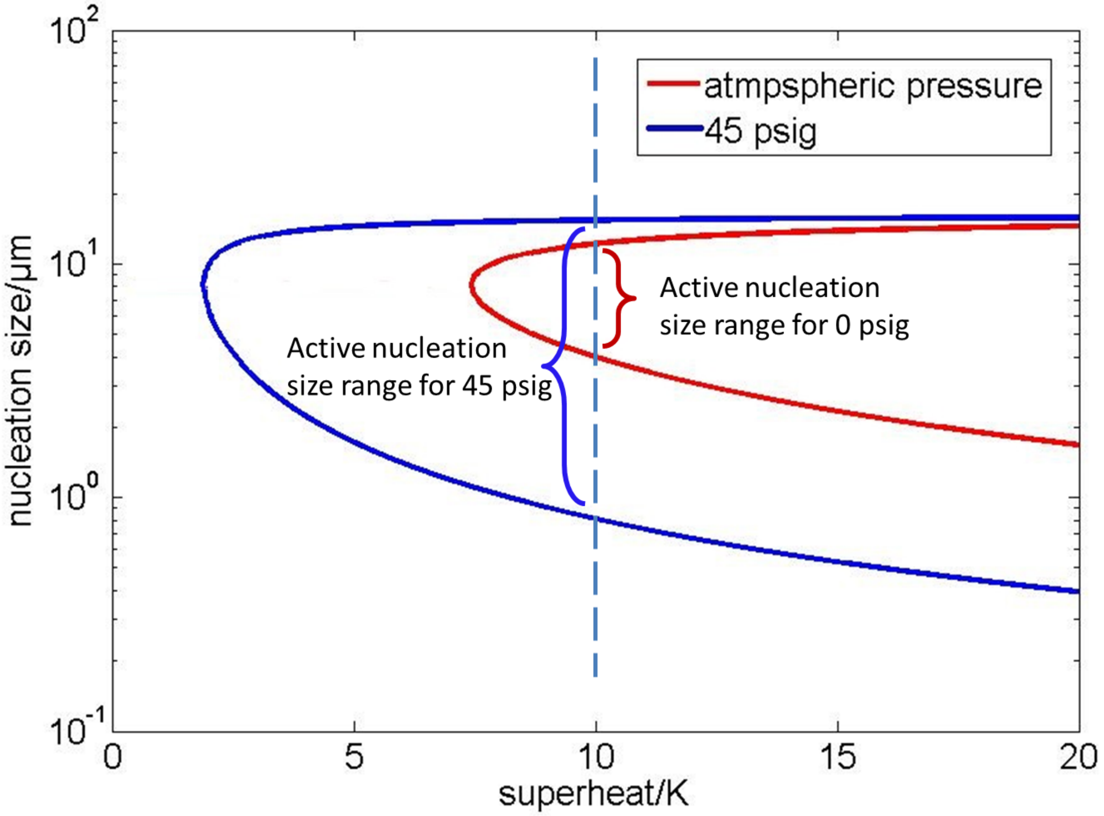

Figure 1.3 Active nucleation size range for boiling of water on copper surface under atmospheric pressure

1.3 Enhanced boiling heat transfer

Increased HTC and CHF will lead to more efficient and compact cooling devices, prevent issues resulting from heater burn out, and save a huge amount of energy. It was reported that 32% increase in CHF will result in 20% increase in power density in pressurized water reactors, which not only increases the safety but also decreases the cost for electric generation [6]. Many variables, such as surface properties, fluid properties, and system pressure, heater size and orientation will affect the performance of pool boiling. In the past, lots of methods have been developed, both active and passive, have been developed to enhance the performance of boiling. Active methods include adding an electric field to the boiling system [7], and vibration of the boiling surface [8]. Passive methods include changing the fluid properties and/or modifying the heated surface properties. In the sections below, passive methods for enhancing pool boiling performance from the literature are summarized and introduced.

1.3.1 Enhancement methods by changing fluid properties

Boiling curves for different fluids are very different because of their own thermal properties. By increasing or decreasing the system pressure, the thermal properties of the fluid are also different resulting in the shift of the boiling curves [8]. The effect of pressure on pool boiling performance will be discussed in detail in Chapter 4. By enhancing the thermal properties of the fluid, the performance of boiling could be greatly enhanced. In recent years, it has been found that the by adding micro/nano scale thermally conductive particles into the boiling fluid can largely increase both the heat transfer coefficient and the critical heat flux.

Popular nano-particles for enhancing boiling performance are Al_2O_3, silica, TiO_2, carbon nanotube, etc. [11-17]. Nanofluids not only exhibit higher heat transfer coefficient, their ability to increase critical heat flux is even more noticeable. Nanofluids usually can increase CHF by 100% to 250% [20]. Factors that affect the enhancement in pool boiling performance include the particle size, the concentration of the nanofluids, and the thickness of the nanoparticle deposition on the heated surface, etc. [18].

For example, Amiri et al. studied the pool boiling heat transfer enhancement using GA-, Cysterinne-, and Ag- treated carbon nanotube dispersed nanofluids, and obtained a CHF increase of 274% [20]. They concluded that the functionalization, the thermal conductivity, and the concentration of the nanofluids play huge roles in the enhancement of CHF. Kathiravan et al. studied multi-walled carbon nanotubes suspension in pure water and water containing 9.0% by weight of sodium lauryl sulphate anionic surfactant. A maximum increase in HTC of 300% was achieved in 1.0% concentration of carbon nanotube nanofluids [23]. Kim et al. studied the mechanism of the increase of CHF of nanofluids [20]. Golubovic et al. experimentally investigated the enhancement of boiling heat transfer and developed analytical model for predicting the CHF [21].

1.3.2 Enhancement methods by engineered surfaces

Boiling heat transfer can also be improved by using enhanced surfaces. Engineered surfaces fabricated by creating micro or nano structures on the surfaces, or deposit coatings to a substrate to change the wettability. Engineered surfaces usually enhance the performance of boiling by increasing the heat transfer area, increasing nucleation sites density, altering bubble departure sizes and frequencies, improving capillary wickability to prevent local “hot spot”.

- **Influence of structured surfaces**

Surface roughness is a key factor in the performance of pool boiling. Roughened surfaces create favorable conditions for bubble formation. Surfaces could be roughened by chemical etching, sanding, or fabricating micro structures such as micro-pins [23-25]. Jones et al. demonstrated that increased surface roughness enhances boiling performance [24].

The advancement in micro-fabrication and surface treatment techniques allow us to design and fabricate more intricate micro or nano structures on surfaces, such as micro-pillared surfaces, micro channeled surfaces, nanoporous surfaces, hierarchically structured surfaces, and so on [25-30]. Different sizes, geometries and configurations of these micro/nano structures play huge role in affecting the boiling heat transfer performance. Previous research has shown that microstructured surfaces increase both CHF and HTC [35]. Studies by Tang et al. and Byon et al. show the ability of porous coated surfaces to enhance boiling [36].

For example, Dong et al. conducted subcooled and saturated pool boiling experiments using ethanol on microstructure and nanostructures and discovered that while microstructured surfaces have higher bubble nucleation density than nanostructured surfaces at low heat fluxes, nanostructured surfaces demonstrate higher capillary wicking, smaller bubble sizes and larger bubble release frequency which all contribute to the delay of CHF [38].

Zou et al. investigated how the critical height of micro/nano structured surfaces affect pool boiling heat transfer. They report a maximum CHF enhancement in CHF of 125% with only 40% increase of surface area on the nano/micro ridged surface. It was found that to the ridges fragment and evaporate the metastable non-evaporating film at the base of a bubble in the contact line thus enhancing the CHF, and only when the ridge is higher than the non-evaporating film will the surface exhibit higher boiling performance [39].

Rahman et al. used biological templates to demonstrate that wickability is the single factor dictation CHF on structured superhydrophilic surfaces. Tobacco mosaic virus was grown on microstructured surfaces and hierarchical surfaces, as shown in Figure 1.4. A CHF of 257 W/cm^2 was reached. The results show that the wickability of the tobacco mosaic virus structure dictates the CHF enhancement [40].

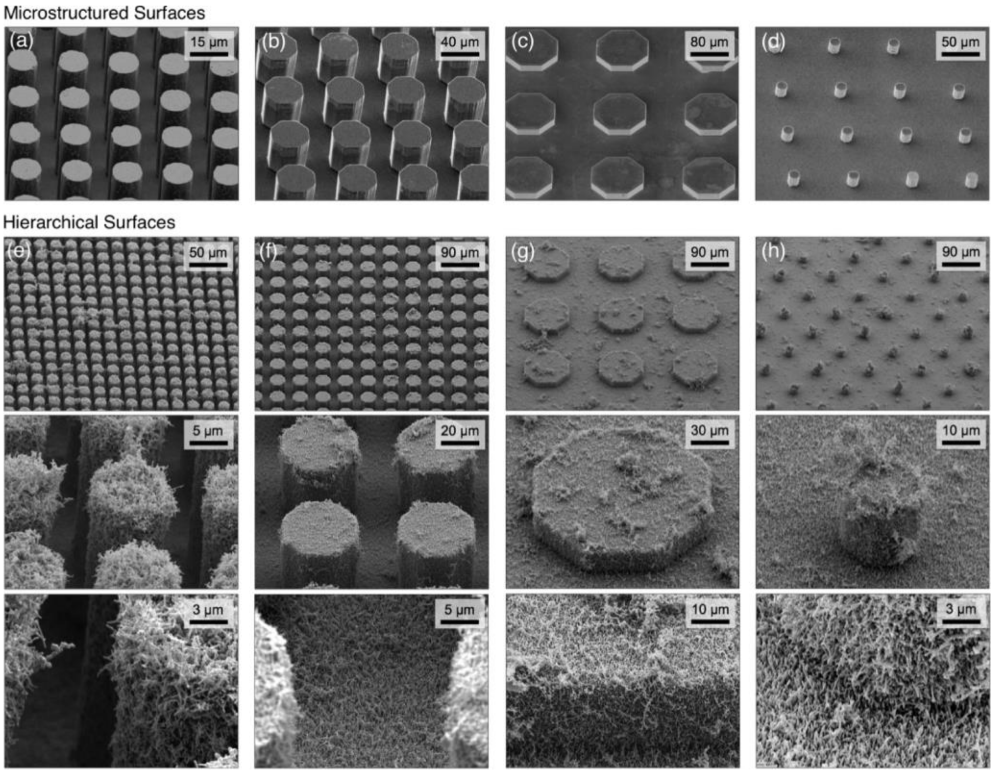

Figure 1.4 Micro, nano, and hierarchically structured silicon surfaces, and TMV coated micro/nano structures from [40].

- **Influence of surface wettability**

There are three ways to modify the wettability of the surface: by changing the surface tension of the liquid, by changing the roughness, and by changing the adhesion tension [41]. Wettability is a very important parameter in predicting HTC and CHF. Higher wettability will enhance the rewetting of the surface preventing local dry spots, and on the other hand, lower wettability will promote bubble formation during the boiling process, increasing the heat transfer coefficient [31-33].

Bourdon et al. performed pool boiling experiment with water on a hydrophilic coated smooth surface and a hydrophobic smooth surface [44]. It was found that with the same topography of the surfaces, the reduction of wettability induces the earlier onset of boiling. The ONB on the superhydrophobic surface is 3.5 C lower than that on the superhydrophilic surface.

Hsu et al. investigated the effects of surface wettability on pool boiling heat transfer [45]. Nano-silica particle coatings were used to vary the wettability of the copper surface from hydrophilic (0˚) to superhydrophobic (149˚). Experimental results show that critical heat flux values are higher in the hydrophilic region while CHF values are lower in the hydrophobic region. Bubble sizes were smaller on the hydrophilic region, and as the wettability decreases, bubble sizes grow bigger.

Feng et al. [41] coated alumina nano coatings on platinum (Pt) micro wires thus decreasing the contact angle of the micro wire to 0˚. A 200% increase in CHF was achieved. It was also found that CHF increases with coating thickness of alumina up to a thickness of 20 nm. It was postulated that the increase in the CHF was due to the enhanced rewetting of the “hot spot”.

In recent years, heterogeneous wetting surfaces has caught many researchers’ attention due to their superb ability to enhance boiling heat transfer. Heterogeneous wetting surfaces have both hydrophobic areas and hydrophilic areas on the same surface. Free heterogeneous wettability can be achieved by creating microstructures on a surface. Patterned heterogeneous wetting surfaces, such as checked heterogeneous wetting surfaces, were also fabricated and studied extensively in the past decade.

Betz et al. and Jo et al. studied the effect heterogeneous wetting surface on boiling heat transfer [47]. It was found that on a hydrophilic surface with hydrophobic dots, the CHF is sustained. At low heat fluxes, the dot size of the hydrophobic dots and the pitch distance between the dots play an important role in controlling the boiling performance. However, the ratio of hydrophobic area to hydrophilic area is not significant in dictating the boiling performance. It was concluded that the increase in boiling heat transfer is due to the continuous bubble generation without waiting time.

1.4 Objectives

In the past, much effort has been done to enhance the performance of boiling. Lots of methods have been proven to be able to increase the heat transfer coefficient and/ or increase the critical heat flux. However, most of these studies were conducted at atmospheric pressure even though a majority of applications in industry are subjected to elevated pressures. Whether these methods are effective at different pressures still needs to be examined.

In this work, a high pressure, high temperature, pool boiling experimental facility was designed and fabricated. The objective of this work is to examine the pressure effect on the pool boiling performances of deionized water on a plain copper surface, a Teflon© coated copper surface, and a graphene oxide coated copper surface. Boiling enhancement mechanism for each surface is discussed.

In order to further understand the heat transfer mechanism of the graphene oxide coated surface, condensation and freezing experiments were conducted to further understand the physical insight of engineered surfaces.

Chapter 2 - Experimental setup

2.1 Overview

This chapter presents a detailed description of the experimental facility for high pressure pool boiling experiments on circular horizontal surfaces. In order to carry out the experiment, the test facility should be able to withstand high pressure and high temperature. The highest pressure designed for the facility is 300 psig (20 bar), which is a pressure that many boiling applications in industry adopt. Since the deionized water is used for all the boiling tests, the highest temperature the boiling vessel should withstand is 350 ˚C, which is the boiling temperature of water at 300 psig. If refrigerant is to be used for the boiling tests under high pressure, 350 ˚C is well above the boiling point of most refrigerants. To achieve high pressure, nitrogen is chosen to pressurize the boiling vessel due to its inert property and low dissolution rate in water even at high pressures. The test surface should be well insulated so that heat loss can be minimized from the side. The entire test surface assembly should also be placed inside the boiling vessel to achieve simple design and simple assembly process. All the heater wires should be outside the boiling vessel to avoid accidental contact with water. The experimental facility is therefore designed based on these requirements. The experimental setup consists four major parts: the boiling vessel, the pressure control system, the heater and power supply, and the data acquisition system. Figure 2.1 is a picture of the entire boiling test facility.

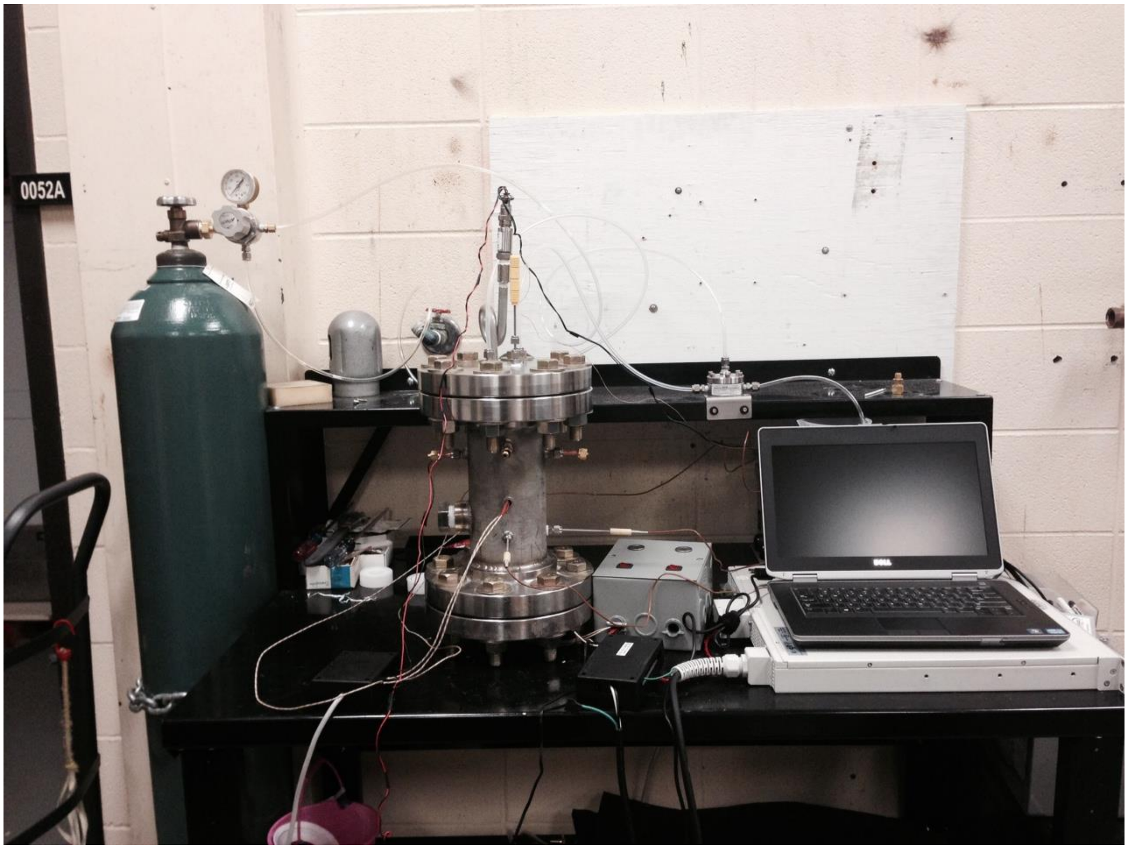

Figure 2.1 Picture of the pool boiling set up

2.2 Boiling vessel

Figure 2.2shows the schematic design of the boiling vessel. To withstand high pressure and high temperature, the boiling vessel is made from 304 stainless steel. The body of the vessel is made from an 11’’ long (27.94 cm), 4’’ (10.16 cm) in diameter stainless steel tube with a wall thickness of 0.375’’ (0.9525 cm). Both ends of the tube are flanged and securely sealed with PTFE (Polytetrafluoroethylene) gaskets. A pressure transducer is mounted on the top flange cap to monitor the pressure inside the vessel during experiments. A siphon offsets the pressure transducer from the high temperature from the inside of the vessel. A K-type thermocouple (Omega) is inserted from the top to measure the bulk temperature of the boiling fluids. Nitrogen is used to pressurize the boiling vessel. The two ports on the top flange cap are inlet and outlet for nitrogen and water vapor. Two 500 W cartridge heaters (Watlow) are inserted from the side of the vessel to preheat water and maintain water at the saturation temperature during the entire experimental procedure. A 500W cartridge heater (Watlow) is inserted from the bottom flange to provide superheat for bubble nucleation. A one-inch diameter high-temperature high-pressure borosilicate glass window is mounted on the vessel to observe bubble nucleation.

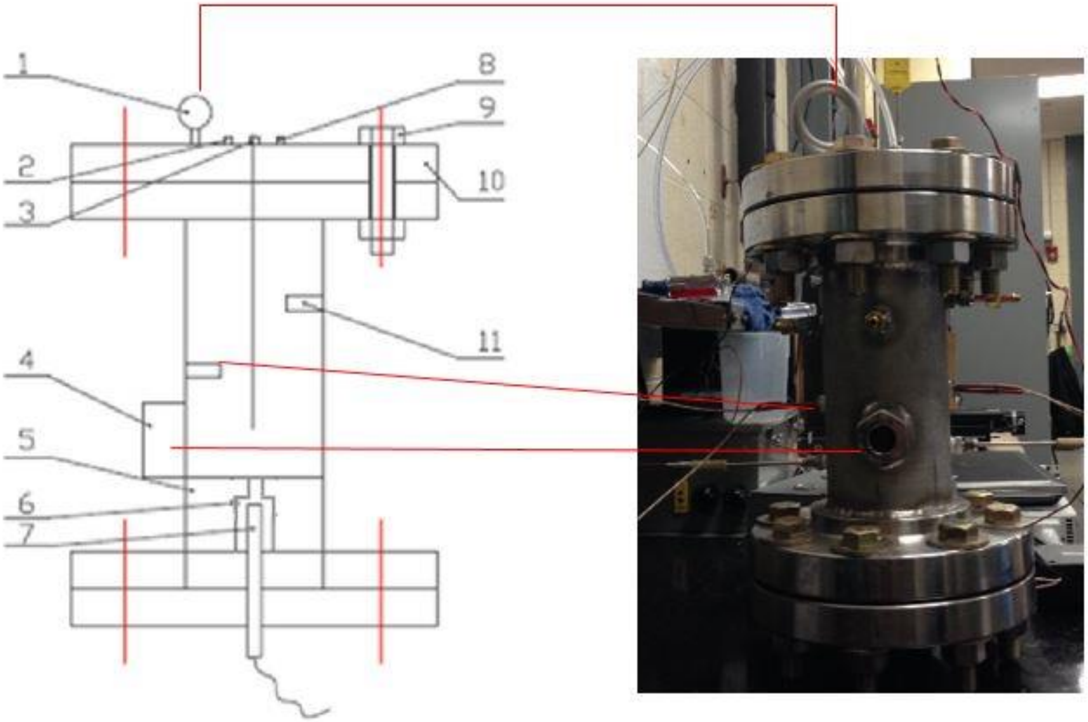

Figure 2.2 Schematic design of the pool boiling vessel. 1. Pressure transducer, 2. Nitrogen inlet, 3. Thermocouple, 4. Viewing port, 5. Heater assembly insulation 6. Copper rod, 7. Auxiliary heater, 8. Nitrogen outlet, 9. Bolt 10. Flange 11. Bulk heater

2.3 Pressure control

Compressed nitrogen is used to pressurize the boiling vessel. Nitrogen is chosen because of its inert property and low cost. Since we are investigating saturated boiling, the effect of dissolved gas on the boiling performance is reduced. Figure 2.3 is a diagram of the pressure regulation system. Nitrogen leaving the nitrogen tank goes through a pressure reducer which is set at the desired system pressure, and is then divided into two lines. One portion of the nitrogen goes to the boiling vessel to pressurize it, and the other portion flows to the back pressure regulator (Equilibar) as a 1:1 control signal for pressure regulation of the boiling vessel. In between the pressure reducer outlet and the vessel inlet port is a gate valve. When water is boiling the gate valve between the nitrogen tank and the boiling vessel is shut down to prevent back flow of vapor. During experiments, the pressure transducer mounted on the top flange reads the system pressure to make sure the pressure is correct. Escaped vapor from the back pressure regulator is collected and manually replenished to the boiling vessel.

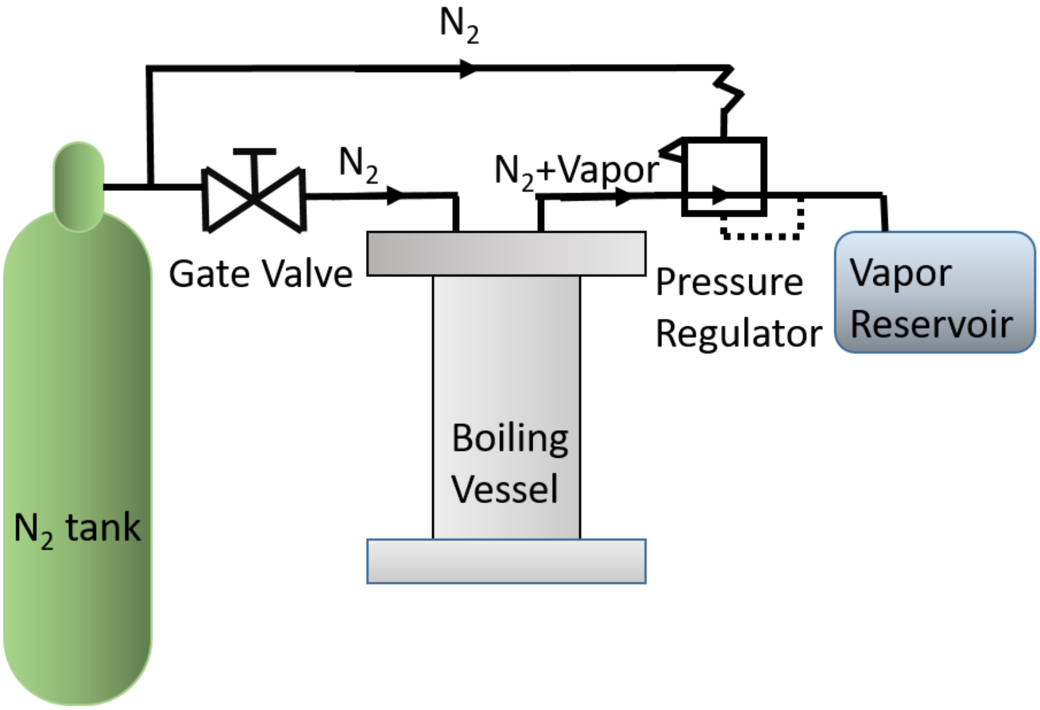

Figure 2.3 Pressure regulation system diagram

2.4 Heater block and insulation

Copper is chosen in this experiment for two reasons. The first reason is that copper has high thermal conductivity, machinability, and wide usage in industry. The second reason is that graphene can easily grow on a copper substrate.

Figure 2.4 is a schematic design of the heated surface block. The top surface of a 3’’ (7.62 cm) long copper rod serves as the heated surface to be studied. The top portion of the copper rod is 11 mm in diameter and 1’’ (2.54 cm) long; the bottom half is 1’’ (2.54 cm) in diameter and 2’’ (5.08 cm) long. This particular dimension is chosen so that the surface area of the heated surface is close to 1 cm2 which is comparable to the surface areas in many other studies in the literature. The top surface is plained by a micro-milling machine and sanded by extra fine sandpaper. The copper rod is insulated with PTFE from both the side and the bottom. The gap between the insulation material and the copper surface is carefully filled with sealant and epoxy and machined smooth to minimize unwanted nucleation sites. Three thermocouple holes are drilled through the boiling vessel, the insulation material to the center of the copper rod. The three thermocouples are 3 mm, 6 mm and 9 mm below the heated surface, respectively. Surface temperature can thus be extrapolated from these readings using Fourier’s law.

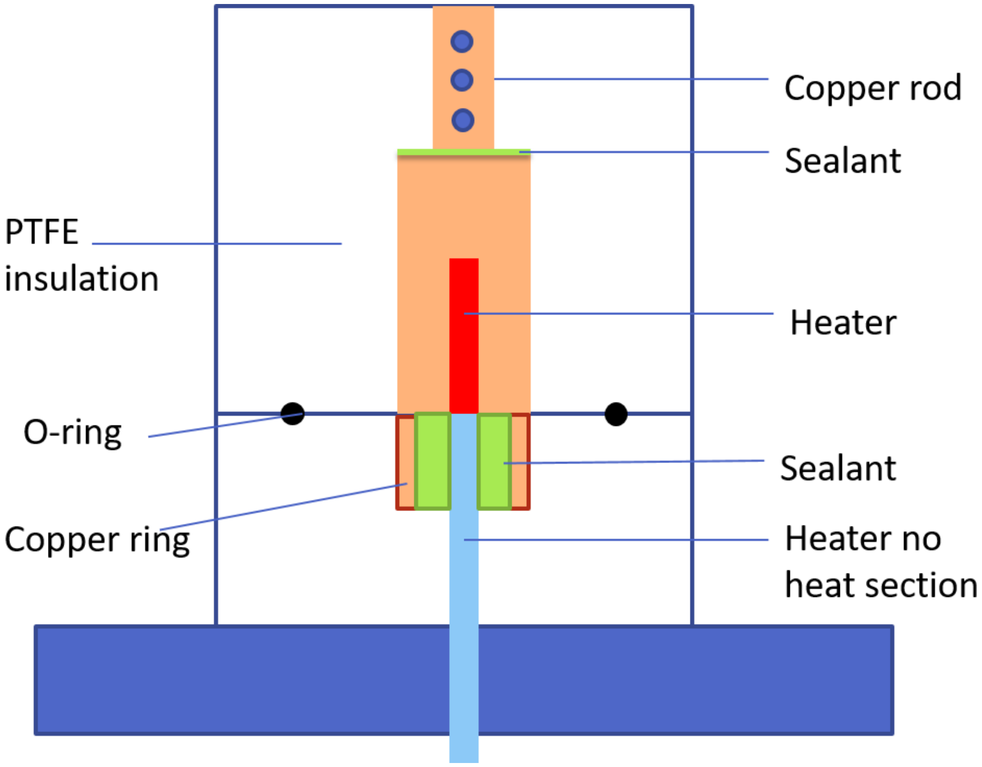

Figure 2.4 Diagram of the heater block deign

A 500W cartridge heater (Waltow), shown in Figure 2.5, inserted in the copper rod from the bottom to provide a heat flux to the heated surface for bubble nucleation. The cartridge heater is designed to have 2.5 in unheated length so that the heated portion of the heater is all inserted to the copper block in order to minimize the heat loss from the lower portion of the heater.

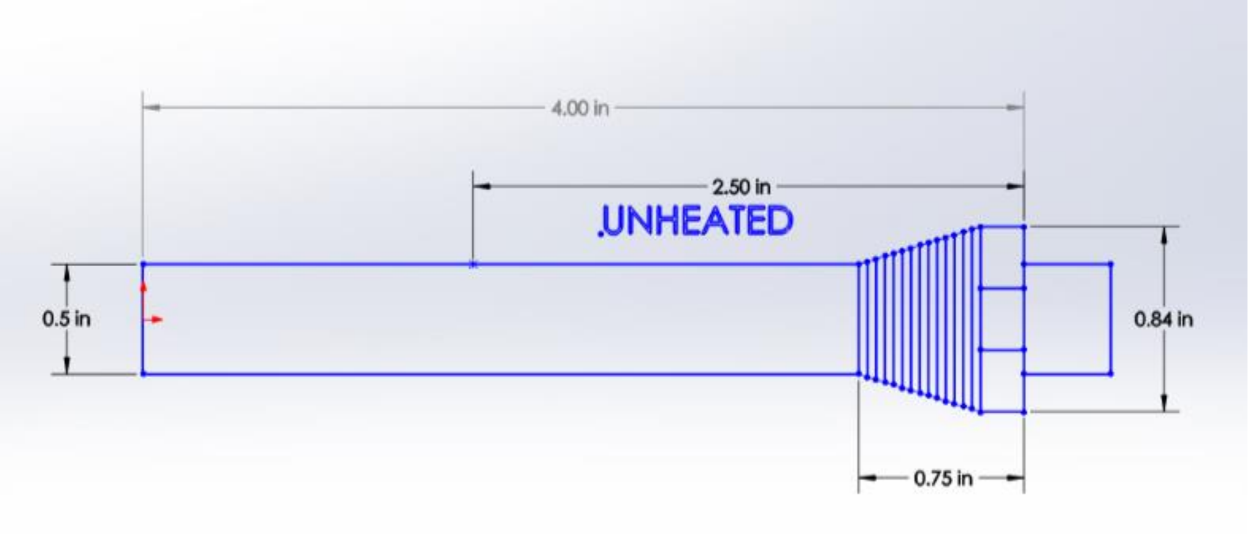

Figure 2.5 Diagram of the auxiliary cartridge heater

To control the heat flux applied to the heated surface, a solid state relay controller, shown in Figure 2.6, is used to alter the duty cycle of the cartridge heaters inserted into the copper rod. The electrical circuit of the SSR controller is shown in Figure 2.6. The SSR controller is powered independently by a 24 V power supply. Duty cycle is controlled by a 0~10 V analog input is chosen for the process controller, where the voltage and the duty cycle time is linearly correlated. For example, 2 V of analog input of the process controller corresponds to 20% working time of the duty cycle, which leads to a heat transfer rate of 100 W to the heated surface.

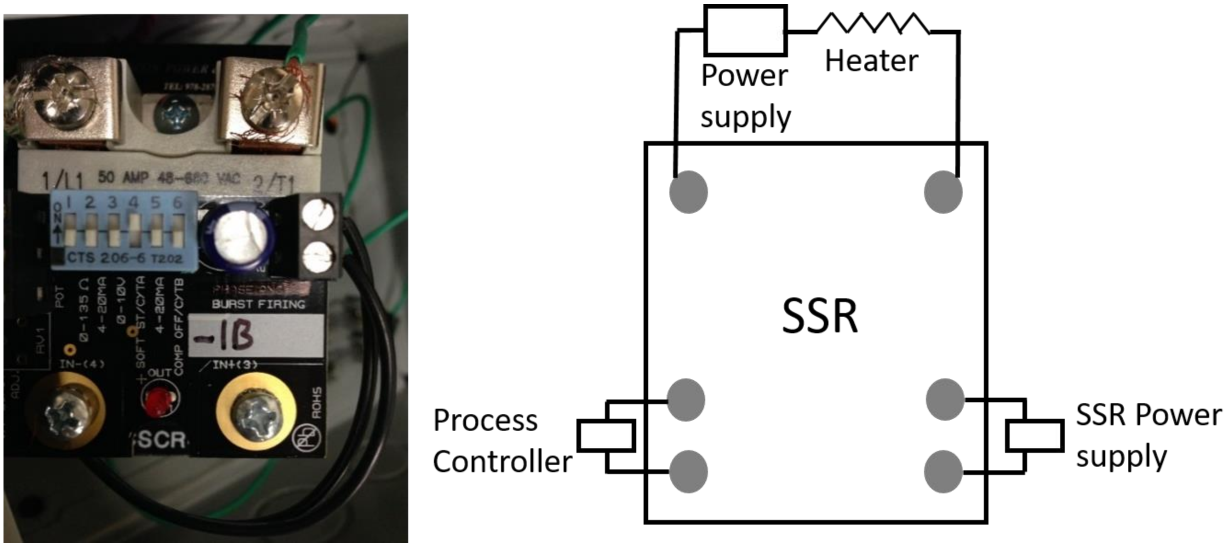

Figure 2.6 Picture of the SSR controller and diagram of the electric circuit

The duty cycle time plot is shown in Figure 2.7. During actual experiments, the duty cycle period is set at one second. This ensures that there is minimum temperature fluctuation to the heated surface, and prolongs the life of the cartridge heater. Heat flux applied to the heated surface is increased from 0 by 1% of the maximum heat flux each time till critical heat flux. In our experiment, this increment is 5 W/cm^2.

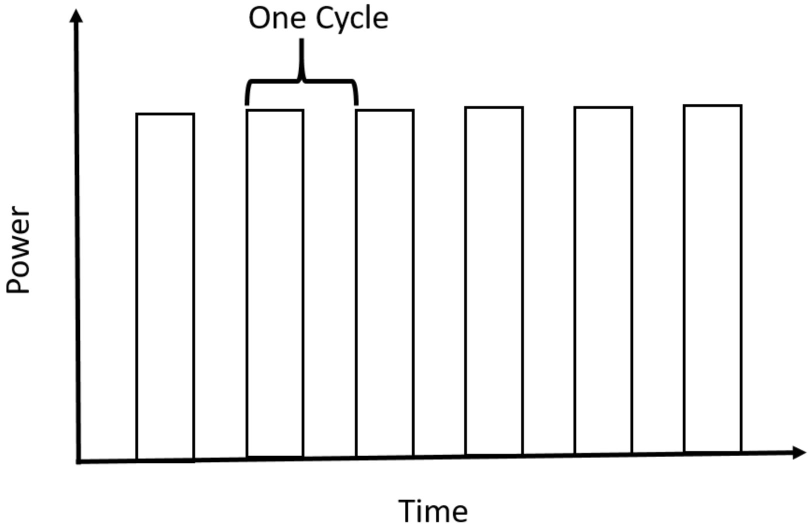

Figure 2.7 Duty cycle time plot

Chapter 3 - Experimental setup

3.1 Experimental procedure

Deionized water is first replenished in the boiling vessel through the ports on the top flange. For experiments at atmospheric pressure, the ports are kept open throughout the experiments. For higher pressure tests, the boiling vessel is pressurized with compressed nitrogen before heating. To set the pressure in the boiling vessel, first adjust the pressure of the pressure reducer at the specified pressure and then open the valve of the nitrogen tank. The pressure transducer on the boiling vessel reads the pressure inside the vessel. After the pressure inside the vessel reaches the desired value, the gate valve between the pressure reducer and the boiling vessel is shut off. Then the boiling vessel is ready for heating. During the experiments, since the back pressure regulator constantly compares pressure inside the boiling vessel and the signal pressure from the pressure transducer, the gas line from the nitrogen tank to the pressure regulator is always open to regulate the pressure inside the vessel all the time. The pressure transducer keeps measuring the pressure inside the vessel throughout the experiment to make sure the pressure is maintained at the desired level.

After the pressure is set at the specified level, water is then heated to saturation temperature with the two 500 W bulk cartridge heaters inside the pool. When it reaches saturation temperature, the duty cycle period is set by setting the voltage signal from the auxiliary power supply, and then the auxiliary heater in the copper rod is turned on to provide wall superheat for bubble nucleation. Each time when increasing the heat flux, the system is allowed to reach steady state before taking measurements. The system is considered to have reached steady state when the temperature change of each thermocouple in the copper rod is less than 1˚C for two minutes. Measurements are taken for one minute for each heat flux. The scan rate of the DAQ is set at 1 Hz, which allows 60 data points for each steady state measurement. The averages of the measured temperatures are used to extrapolate the heater surface temperature. After each test, the gate valve between the nitrogen tank and the boiling vessel is opened again to replenish nitrogen until the water temperature drops under 100 °C. This prevents the sudden evaporation of high temperature water at lower pressures. A gear pump is used to remove water from the boiling vessel after the boiling tests.

3.2 Data reduction

The independent variables in each experiment are the heat flux applied to the heated surface and the system pressure. The dependent variables are the four temperature measurements: the bulk fluid temperature, and the three temperature measurements from the heater block. Heat flux is calculated by dividing the power of the heater by the area of the heated surface, as shown in the equation below

$$q'' = \frac{q}{A} \qquad \text{Eq. 3.1}$$

Where $q''$the heat flux, q is is the heat supplied by the auxiliary heater, and A is the area of the heated surface.

Temperature of the heated surface is extrapolated by the three temperature readings from the copper heater block using the Fourier’s law shown in the equation below.

$$q'' = -k\frac{\Delta T}{\Delta x} \qquad \text{Eq. 3.2}$$

Where $q''$the heat flux, k is is the thermal conductivity of copper, ΔT is the wall superheat, and Δx is the distance between each neighboring thermocouple holes.

Below is one set of sample data from the boiling test at atmospheric pressure on the plain copper surface at 30 W/cm^2, where T_0 is the temperature of the bulk fluid, T_1, T_2 and T_3 are the three thermocouples readings inside the copper rod respectively from top to bottom.

Table 3.1 Sample data at atmospheric pressure on the plain copper surface at 30 W/cm^2

	T_0	T_1	T_2	T_3
Temperature readings (˚C)	98.7	114.7	118.5	124.7

To extrapolate the surface temperature, linear regression tool in excel is used as shown in Figure 3.1. The x-axis is the distance between the thermocouple holes and the surface, and the y-axis is the temperature readings. By doing the linear extrapolation, the surface temperature of the plain copper surface at 30 W/cm^2 is 111.8 ˚C. The difference between the extrapolated surface temperature and measured bulk fluid temperature is calculated to be 13.1˚C, which is the wall superheat at 30 W/cm^2 heat flux.

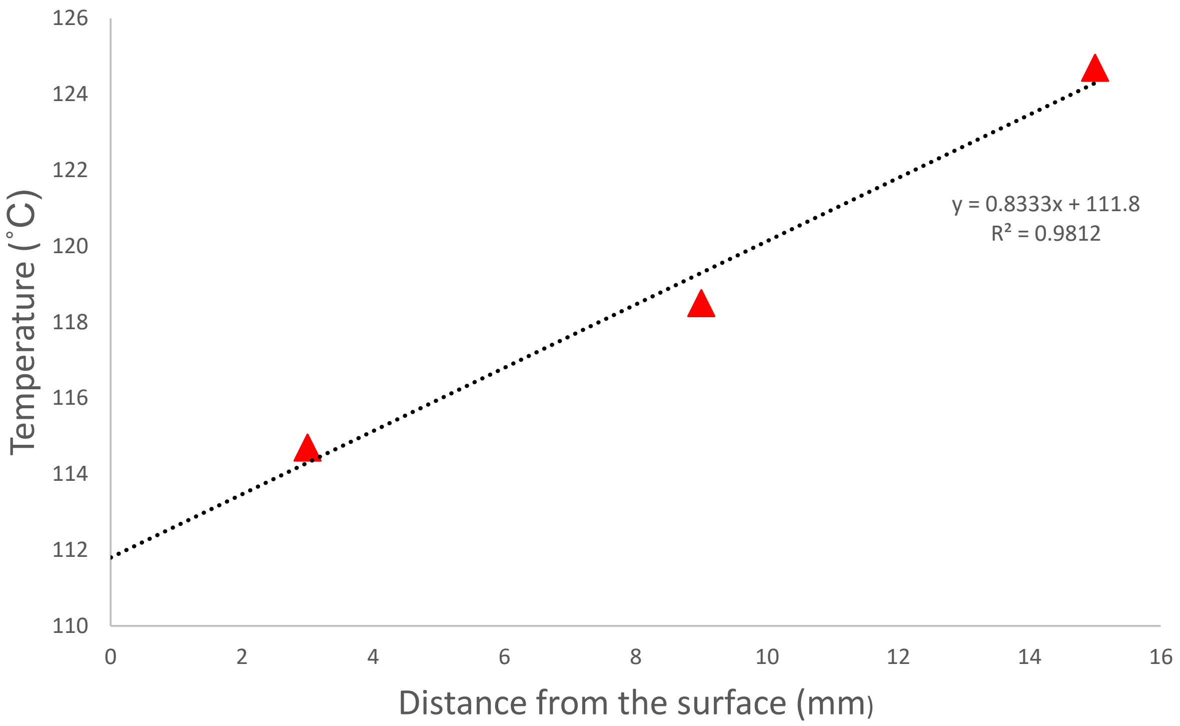

Figure 3.1 Sample surface temperature extrapolation

3.3 Uncertainty analysis

The pressure transducer measurement, the thermocouple measurements and the heat losses all contribute to the uncertainty of the experimental result. K-type thermocouples are used in this work. The error of the thermocouple reading is ±1.1 K. All thermocouples are calibrated at 0 °C and 100 °C before the tests to reduce bias errors. The pressure transducer error is 16.75 μV, which is 0.08375 psi (577.5 Pa). Heat loss from the auxiliary heaters was calculated are using the measured temperature gradient. For example, for 30 W/cm^2 applied heat flux on the plain copper surface at atmospheric pressure data set, by using Eq. 3.1, the actual heat flux is calculated to be 25.7 W/cm^2. The heat loss is therefore 14%. Uncertainty of the heat flux, and heat transfer coefficient are calculated using Eq. 3.3.

$$U = \sqrt{\sum_{i=1}^{n}(\frac{\partial P}{\partial a_i}U_{ai})} \qquad \text{Eq. 3.3}$$

Where U is the uncertainty, P is the parameter, a_i is the measured parameter. The average error from the applied heat flux range from 1% to 23%.

Chapter 4 - Effect of pressure on plain copper surfaces

4.1 Introduction

Pressure has a huge effect on the boiling performance because of the change in the thermal properties of the working fluid [8]. As shown in Figure 4.1, within the range of our experiment, both the latent heat of vaporization and the change on specific volume decreases with the increase of pressure. Other fluid properties, such as surface tension, saturation temperature also play a huge role in affecting the bubble nucleation behavior in a boiling process. Table 4.1 summarizes the thermo-fluid properties of water from 1 bar to 4 bars.

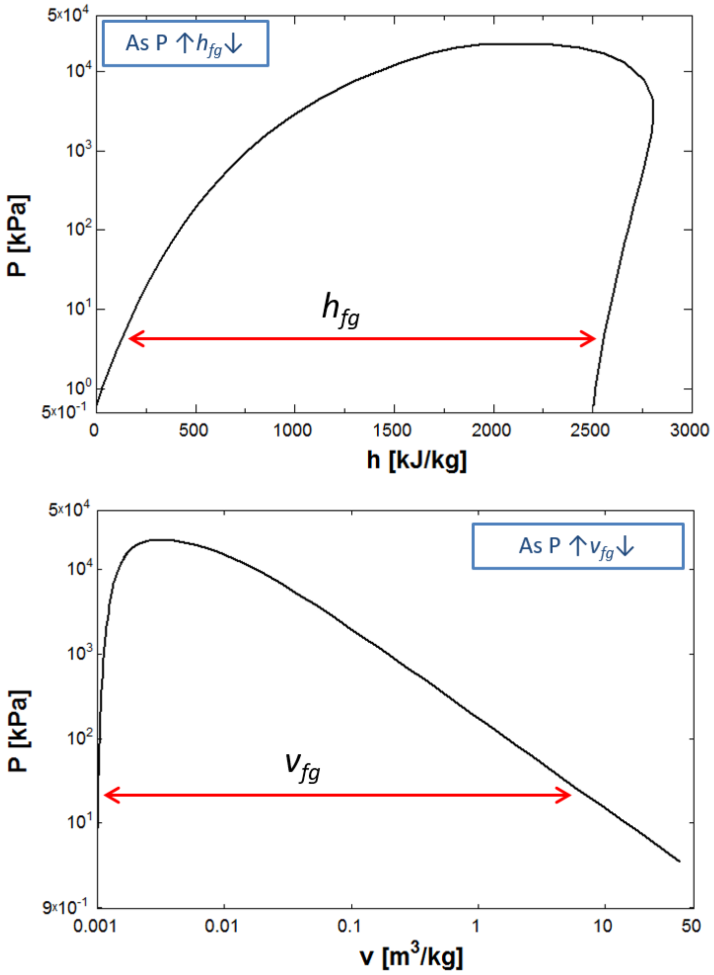

Figure 4.1 Effect of pressure on specific volume and enthalpy of water.

Table 4.1 Thermo-fluid properties of water

P(bar)	σ (N/m)	T_{sat} (K)	ρ_v (kg/m^3)	ρ_l (kg/m^3)	h_{fg} (J/kg)
1	0.0589	372.6	0.590	958.589	2258000
2	0.0546	393.2	1.129	942.951	2201900
3	0.0520	406.6	1.650	931.792	2163800
4	0.0505	416.6	2.162	922.849	2133800

In the past, large amount of effort has been made for developing correlations and analytical models for predicting bubble nucleation site density, bubble departure diameter, bubble release frequency, heat transfer coefficient and critical heat flux **Error! Reference source not found.**. In the Fritz's model, bubble departure diameter is correlated with the buoyancy force of a bubble and the surface tension force as shown in Equation 4.1 [48],

$$D_d = 0.0208\theta\left[\frac{\sigma}{g(\rho_l - \rho_g)}\right]^{1/2} \qquad \text{Eq. 4.1}$$

where D_d is the bubble departure diameter, θ is the contact angle, σ is the surface tension, g is the gravity, ρ_l and ρ_g are the density of the liquid and vapor respectively. A bubble departs the heated surface when the buoyancy force of the bubble is larger than the surface tension force.

Mikic and Rohsenow developed correlations for active nucleation densities for commercial surfaces in the partial nucleate boiling regime [48].

$$n_a' = \left[\frac{D_s}{\frac{4\sigma T_{sat}}{\rho_v h_{fg}\Delta T_w}}\right]^m \qquad \text{Eq. 4.2}$$

where m is the empirical constant, D_s is the largest cavity diameter on the surface, σ is the surface tension of the fluid, T_{sat} is the saturation temperature of the liquid, ρ_v is the vapor density, h_{fg} is the latent heat of vaporization, and ΔT_w is the wall superheat.

The bubble release frequency can be expressed using Zuber's correlation [48],

$$fD_d = 0.59\left[\frac{\sigma g(\rho_l - \rho_g)}{\rho_l^{\;2}}\right]^{\frac{1}{4}} \qquad \text{Eq. 4.3}$$

where f is the bubble release frequency, D_d is the bubble departure diameter σ is the surface tension, , g is the gravity, and ρ_l and ρ_g are the density of the liquid and vapor respectively.

Due to the change in the thermo-fluid properties of water as the system pressure increases, bubble nucleation behavior is quite different at different pressures. Using the correlations above, the percent of increase in active nucleation site density, bubble departure diameter and bubble release frequency is plotted in Figure 4.2 against pressure from 1 bar to 4.37 bar, which is the pressure range in this work. As pressure increases from 1 bar to 4.37 bar, the active nucleation site density increased by 99.1%, the bubble departure diameter decreased by 6.5%, and the bubble release frequency increased by 4.3%.

Based on vapor liquid exchange model, Forster and Greif developed a model for predicting the heat transfer coefficient as shown in Eq. 4.4 [49],

$$\mathrm{HTC} = \beta D_d^2 f^{1/2} n_a^{'} \qquad \text{Eq. 4.4}$$

where $\beta=2(\pi k_l \rho_l c_{pl})^{1/2}$, D_d is the bubble departure diameter, f is the bubble release frequency, and n_a' is the active nucleation site density. By plugging in the calculated results for all the parameters in Eq. 4.4 for both 1 bar and 4.37 bars, the increase in the heat transfer coefficient is predicted to be 70.1% from 1 bar to 4.37 bars.

Zuber also developed an analytical for model for estimating the critical heat flux of water. It is assumed that the occurrence of CHF is due to the Kelvin-Helmholtz instabilities [50].

$$\text{CHF}=\frac{\pi}{24}\sqrt{\rho_v}[h_{lv}][\sigma g(\rho_l-\rho_v)]^{1/4} \qquad \text{Eq. 4.5}$$

where h_{lv} is the latent heat of vaporization, σ is the surface tension, g is the gravity, ρ_l and ρ_v are the density of the liquid and vapor respectively. According to this correlation, CHF of water for a highly wetting surface should occur at 110 W/cm^2.

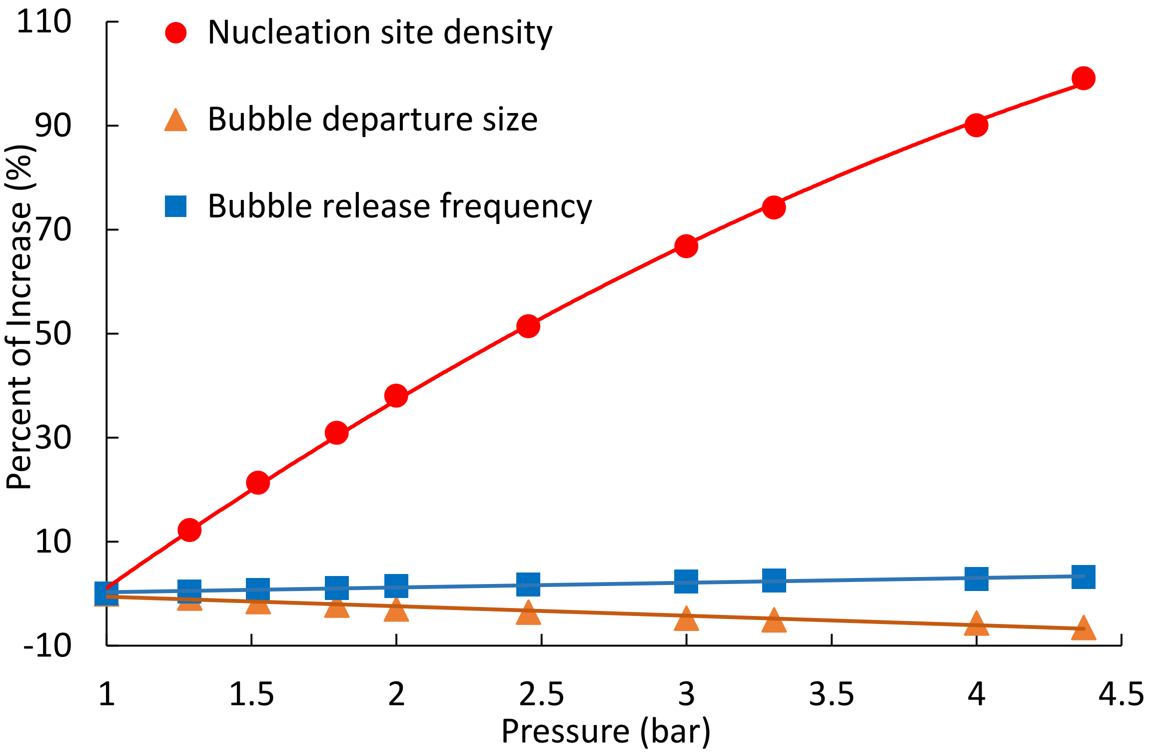

Figure 4.2 Percent of change in bubble nucleation site density, bubble departure size and bubble release frequency with the increase of pressure

Lots of experimental work has also been reported in the literature investigating the effect of pressure on the performance of boiling. Laca et al. conducted saturated pool-boiling experiments at one atmosphere and sub-atmospheric pressure on fine filament screen-laminate enhanced surfaces. Experiments were conducted on vertically oriented copper test surfaces in saturated distilled water at pressures of 0.2 atm., 0.3 atm., 0.5 atm., and 1 atm. It was found that boiling performance can be significantly improved by application of a multiple layer fine filament screen laminate to the heat transfer surface. An enhancement of up to 22 times that of the unenhanced surface was obtained at a superheat of 8K and a pressure of 0.2 atm [51]. Seo et al. investigated, the pool boiling heat transfer characteristics in deionized water under atmospheric pressure on SiC cladding and compared the results to zircaloy-4 cladding. The experimental results showed a 63% higher CHF for the SiC heaters than the zircaloy heaters [52]. Giraud et al. studied the specific characteristics of water pool boiling in narrow channels at subatmospheric pressure in order to acquire the fundamental knowledge needed to improve the design of compact evaporators in these sorption systems [53]. McGrills et al. studied several horizontal heated surface structures’ ability to enhance saturated boiling at low pressures [54]. Das et al. studied boiling on horizontal tubes at moderate pressures [55]. More data is needed to determine heat transfer performance enhancement at higher pressures on modified horizontal surfaces.

In this chapter, the pressure effect on a plain copper surface is examined at four different pressures: atmospheric pressure, 15 psig, 30 psig and 45 psig. These pressures fall in the range of normal operation of domestic boilers. The results also serve as a foundation for future studies on the pressure effect on engineered surfaces.

4.2 Results and discussion

The results of the pressure effect on pool boiling performance of plain copper surfaces are shown in Figure 4.3. As the pressure increases, the boiling curves shift to the left, indicating a high heat transfer coefficient which is consistent with previous findings in the literature. The critical heat flux also increases with the pressure. Moreover, the onset heat flux of nucleation also increases with the pressure. Critical heat flux for the plain copper surface was found to be 85 W/cm^2 at atmospheric pressure, 100 W/cm^{2}at 15 psig (205 kPa), 110 W/cm^2 at 30 psig (308 kPa) and 45 psig (412 kPa). Accoding to Zuber's theory, CHF is positively proportional to pressure. The experimental results show the same trend as predicted in the Zuber's theory.

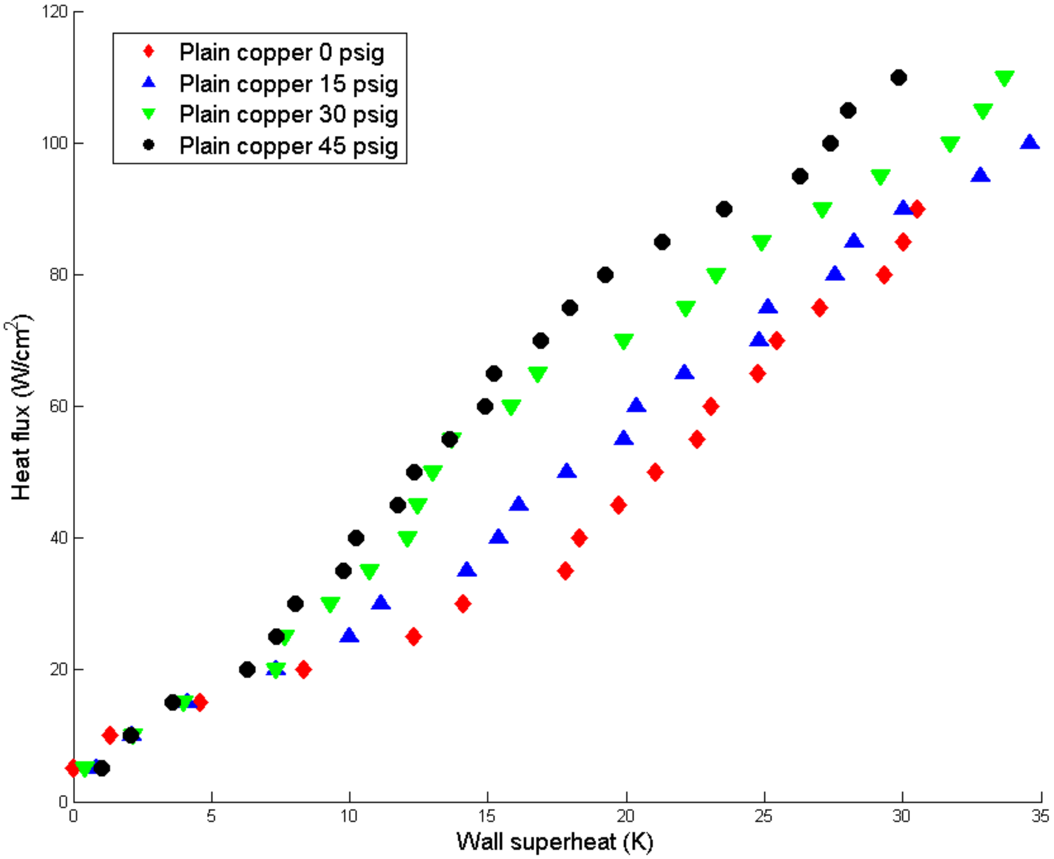

Figure 4.3 Boiling curves on the plain copper surface at different pressures

Heat transfer coefficient is plotted against heat flux in Figure 4.4. Heat transfer coefficient data at very low heat fluxes (<10 W/cm^2) is omitted due to the large error in measurements. It is shown in the plot that the heat transfer coefficient increases as pressure increases. The average heat transfer coefficient increased by 100% from atmospheric pressure to 45 psig.

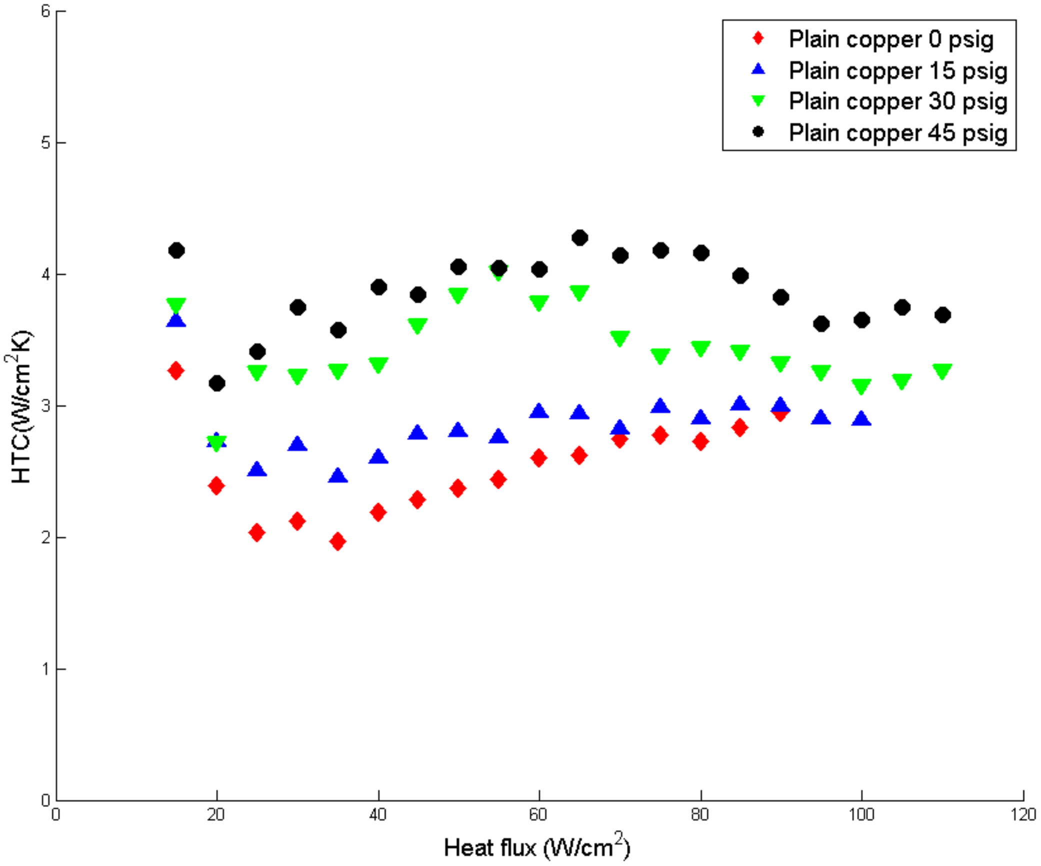

Figure 4.4 Heat transfer coefficient vs. heat flux on the plain copper surface at different pressures

Figure 3.5 shows the contact angle of water on the plain copper surface, and the bubbles leaving the heated copper surface at atmospheric pressure. The bubble departure diameter on the copper surface at atmospheric pressure is around 2.6 mm. Bubble sizes were observed to be decreasing as the pressure increased. Both the increase in the heat transfer coefficient and the critical heat flux is explained by the decreased bubble departure sizes at higher pressures. The change in the bubble size is due to the change in the thermal property of water at higher pressures. As discussed in the previous section, differences of specific heat between liquid and vapor decreases as pressure increases, thus the bubble sizes are smaller at higher pressures. Smaller bubble sizes forming on the heated surface discourages coalescence of bubbles on their neighboring sites and allows more nucleation sites. This results in the higher efficiency in removing heat from the surface and the delay in critical heat flux.

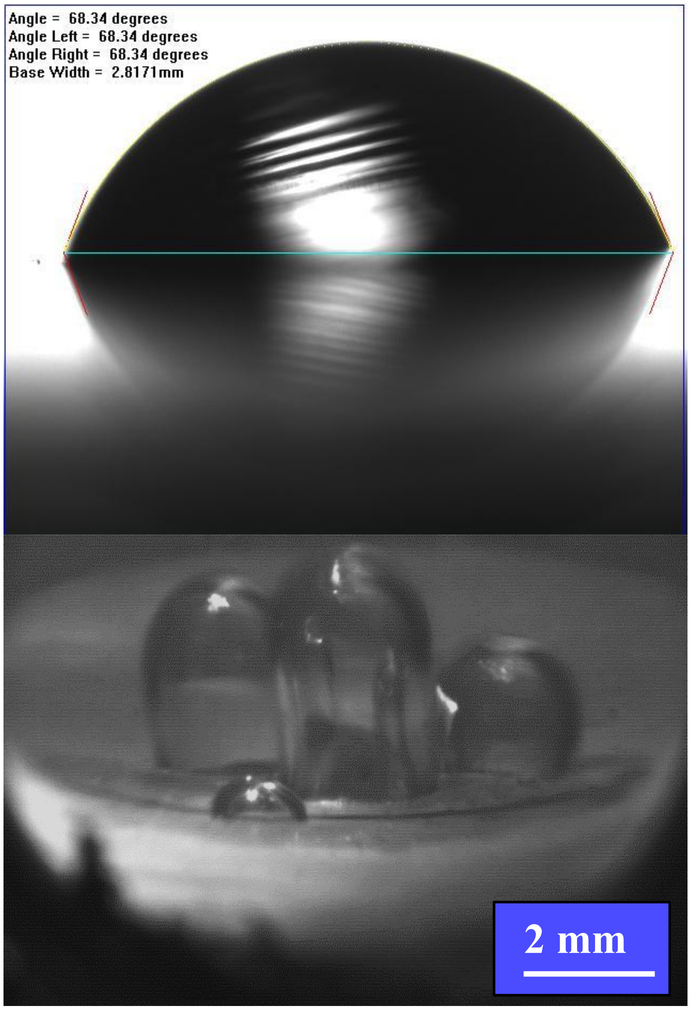

Figure 4.5 Contact angle of water on the plain copper surface (left); Bubbles leaving the heated copper surface at atmospheric pressure (right)

4.3 Conclusions

In this chapter, boiling performance on a plain copper surface was examined at four different pressures: atmospheric pressure, 15 psig, 30 psig, and 45 psig. It can be concluded that

- Heat transfer coefficient and critical heat flux of water on the plain copper surface is positively proportional to the pressure.
- Bubble sizes decrease as pressure increases on the plain copper surface.
- The enhancement in the boiling heat transfer performance is due to the change in the thermal properties of water at higher pressures.

Chapter 5 - Effect of pressure on hydrophobic surfaces

5.1 Introduction

Surface wettability is an important parameter in determining the boiling heat transfer. Surface wettability can be represented by contact angle, which is the angle between the liquid-air interface and the solid as shown in Figure 5.1. A surface is called hydrophobic when the contact angle of water on the surface is larger than 90˚, and hydrophilic when the contact angle is smaller than 90˚.

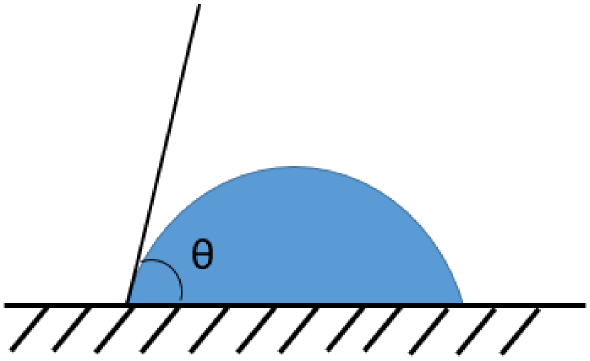

Figure 5.1 Contact angle of liquid on a solid surface

Previous research has shown that surface wettability greatly affects the pool boiling performance. It was found that hydrophilic surfaces increase the critical heat flux due to their ability to rewet the surface after the departure of boiling. In contrary, hydrophobic surfaces increase heat transfer coefficient at low heat fluxes for it requires less energy for bubbles to grow. Larger sizes of bubbles are previously reported. However, bubble sizes are smaller at higher pressures as discussed in the previous section. How heat transfer will be affected by pressure on a hydrophobic surface is unclear. In this chapter, pool boiling experiments on a Teflon© coated copper surface at two different pressures are examined.

In this chapter, Teflon© solution was coated on a copper substrate to decrease the wettability of the surface. The performances of boiling on the hydrophobic Teflon© coated copper surface and on a plain copper surface were examined and compared under atmospheric pressure and 15 psig.

5.2 Surface preparation

Teflon© is coated on the top surface of the copper cylinder using dip coating. The Teflon© solution was made by combining 1 part of the Teflon AF solution with 24 part of refrigerant FC-40. Before dip coating, the copper substrate was soaked in isopropanol and then cleaned in the ultrasonic cleaner for 20 minutes. After cleaning, the copper substrate was dipped in the Teflon©/refrigerant solution, and air dried. Then the copper substrate was baked in the oven at 165˚C overnight. This method has been reported in the literature to create a uniform layer of Teflon® coating of approximately 260 nm in thickness [56].

Static contact angles of water on both the plain copper surface and the Teflon© coated copper surface are measured using a static goniometer. Average static contact angle on the Teflon© coated surface is 117°, while the average contact angle on the plain copper surface is 68°. Figure 5.2 are pictures of water droplets on the plain copper surface and Teflon© coated copper surface.

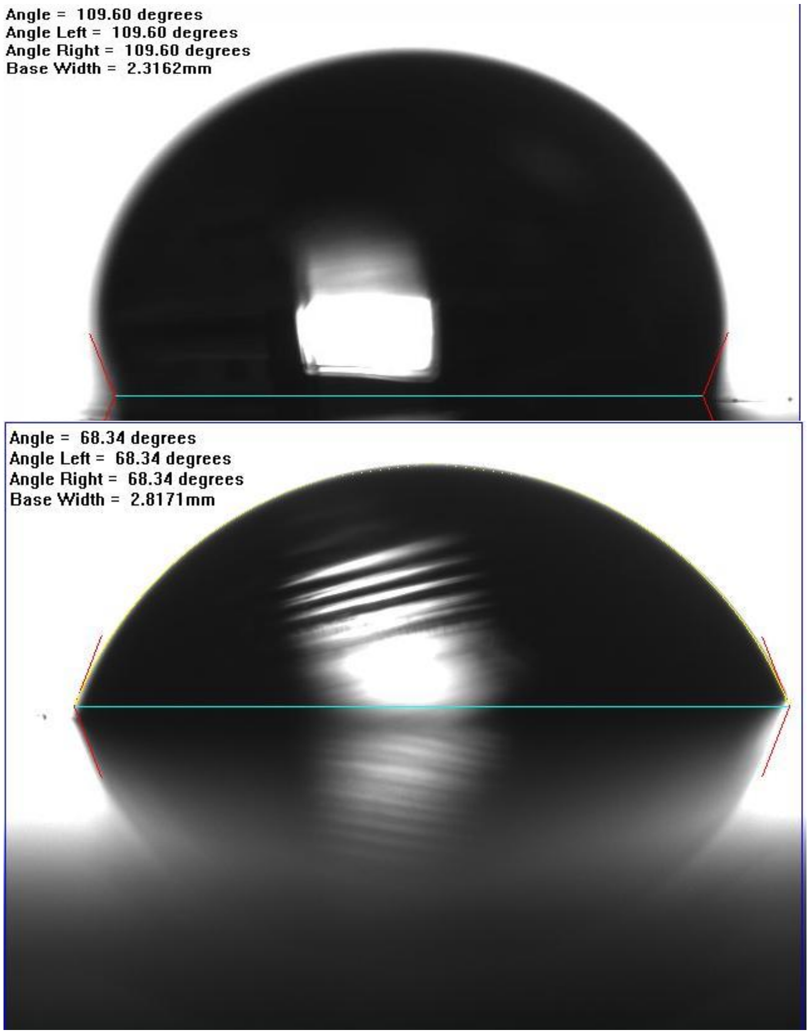

Figure 5.2 Contact angle of water on the Teflon© coated copper surface (left), and on the plain copper surface (right)

Temperature drop due to the thermal resistance of the coated layer at 50 W/cm^2 is calculated to be 0.657 K using the following equation. The temperature difference is considered insignificant compared with the surface temperature of the copper during each test.

$$\Delta T = \frac{q''\cdot L}{k \cdot A} \qquad \text{Eq. 5.1}$$

Where ΔT is the temperature difference, q'' is the applied heat flux, L is the thickness of the Teflon© coating, k is the thermal conductivity of the Teflon© coating, and A is the coated surface area.

5.3 Results and discussion

Boiling tests of deionized water are conducted on the plain copper at 0 psig, 15 psig and 22 psig, and on the Teflon© coated surface at 0 psig and 15 psig. CHF is not reached in these tests. Figure 5.3 shows all the boiling curves for each pressure on both surfaces. The boiling curves are shifted to the left at increased pressure on both surfaces due to the change in the water properties as discussed in the previous chapter. At the same pressure, the heat transfer coefficient of the Teflon© coated copper surface is higher than the plain copper surface. At lower heat fluxes (<50 kW/m^2), pressure effect on the heat transfer coefficient is negligible. Since fewer bubbles form at lower heat fluxes, natural convection is the dominant mode of heat transfer on the heated surface. With few bubbles forming on the surface, the effect of pressure on boiling heat transfer is not significant. At higher heat fluxes (>50 kW/m^2), more bubbles form on both surfaces. Since the energy that the bubbles need to overcome at different pressures is a function of the fluid property, the effect of pressure is more significant at higher heat fluxes.

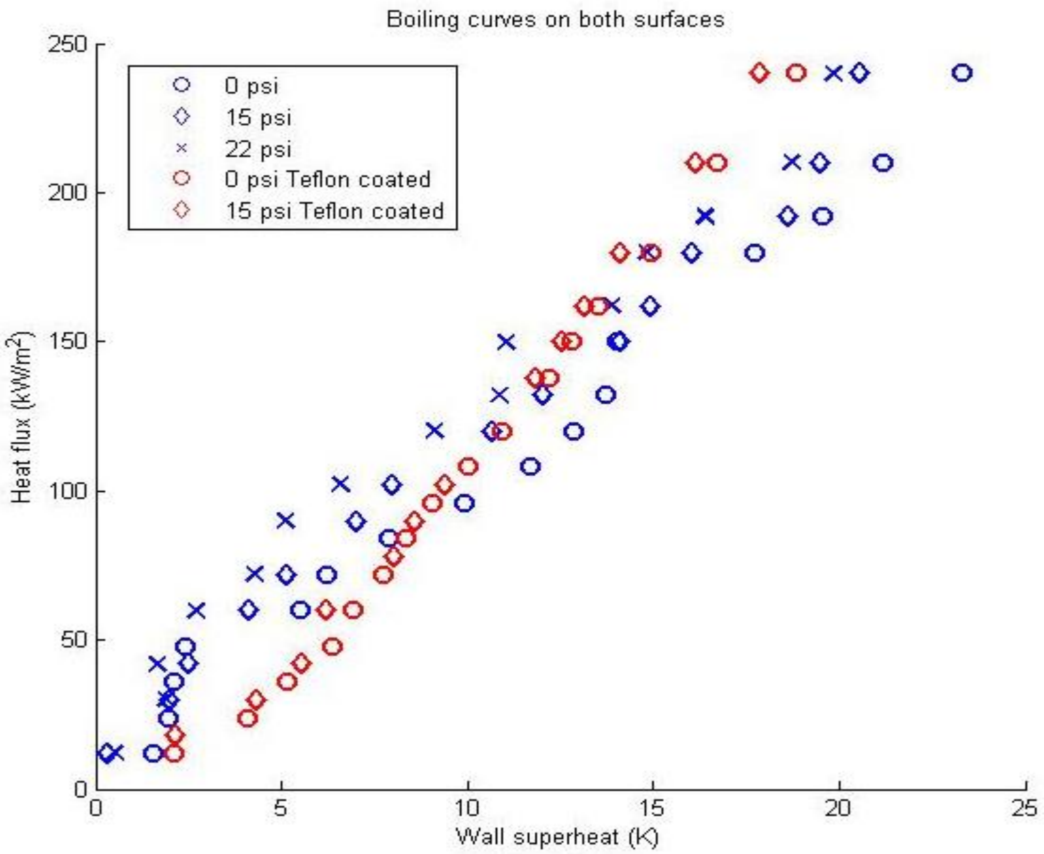

Figure 5.3 Boiling curves of water on Teflon coated copper surface and plain copper surface at different pressures

Bubble dynamics are drastically different on both surfaces. On the hydrophobic surface, average bubble sizes are larger than that on the plain copper surface, but the nucleation sites are fewer than that on the plain copper surface. Figure 5.4 is a comparison of the bubble departure size on both surfaces at atmospheric pressure. On the plain copper surface, the bubble departure size is 2.6 mm, and on the Teflon© coated surface, the bubble departure size is 3.7 mm. The increase in the bubble departure sizes is caused by the decreased wettability of the hydrophobic surface.

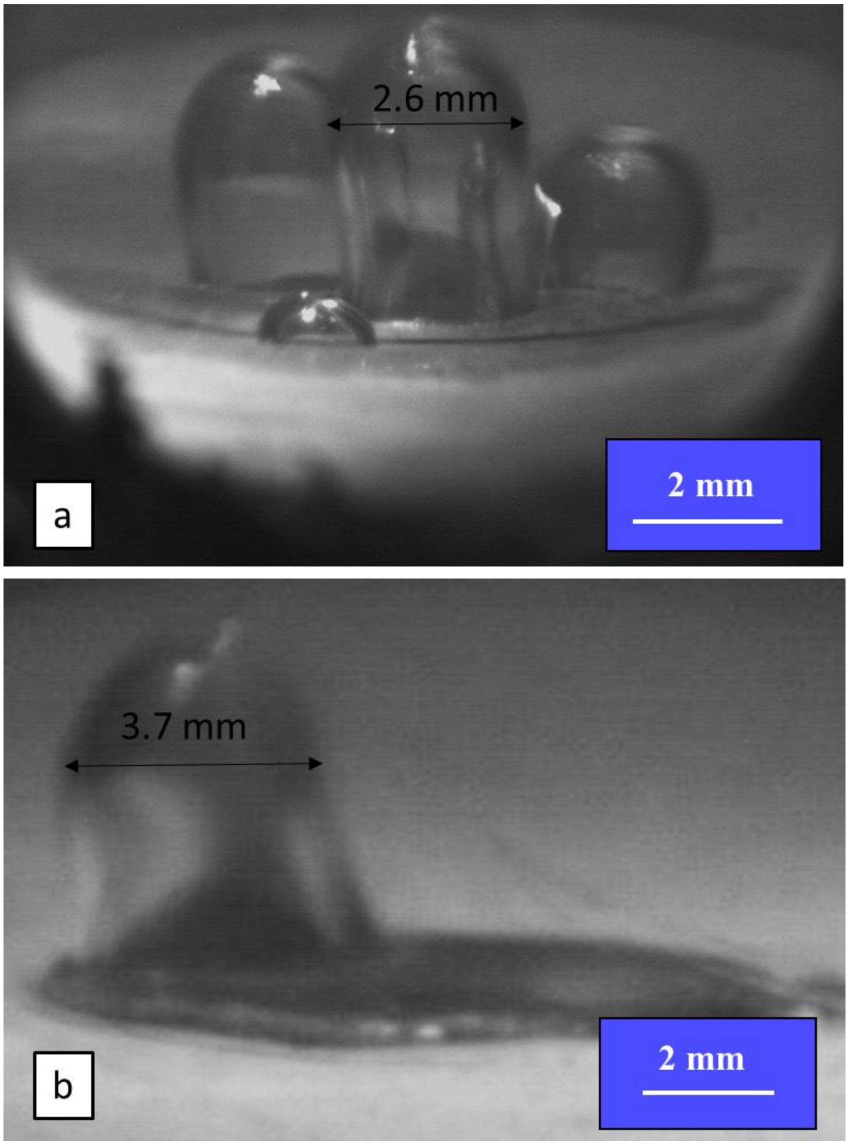

Figure 5.4 Bubbles forming on the plain copper surface (a) and on the Teflon coated surface (b)

It should also be noted that on the copper surface, the average heat transfer coefficient increased by 20% from 0 psi to 15 psi. However, on the Teflon© coated copper surface, the average heat transfer coefficient increased only by 14% from 0 psi to 15 psi. This demonstrates that the wettability of the heated surface has a higher impact than the fluid property change. As the pressure increases, bubble size should decrease. On the other hand, hydrophobic surface promotes larger size bubbles. The competing effect between the pressure and the wettability resulted in the smaller change in heat transfer coefficient on the Teflon© coated hydrophobic surface due to the increase in pressure.

Figure 5.5 and Figure 5.6 show the heat transfer coefficient enhancement on Teflon© coated surface at two pressures. At low heat fluxes (<50 kW/m^2) side bubbles forming around the gap of between the heated surface and the insulation material has a huge impact on the heat transfer behavior, which results in large heat transfer coefficient. When the heat flux reaches approximately 80 kW/m^{2,} the heat transfer coefficient of water on the Teflon© coated surface shows a great increase. At atmospheric pressure, the average heat transfer coefficient is 14 kW/m^{2}K on the Teflon© coated hydrophobic surface, and 9.6 kW/m^{2}K on the plain copper surface. An increase of 46% in heat transfer coefficient was achieved on the hydrophobic surface. At 15 psi, the average heat transfer coefficient is 16 kW/m^{2}K on the Teflon© coated hydrophobic surface, and 12 kW/m^{2}K on the plain copper surface. An increase of 33% in heat transfer coefficient was achieved on the hydrophobic surface. The increase in heat transfer coefficient on the hydrophobic surface is explained by the larger bubble sizes forming on the surface.

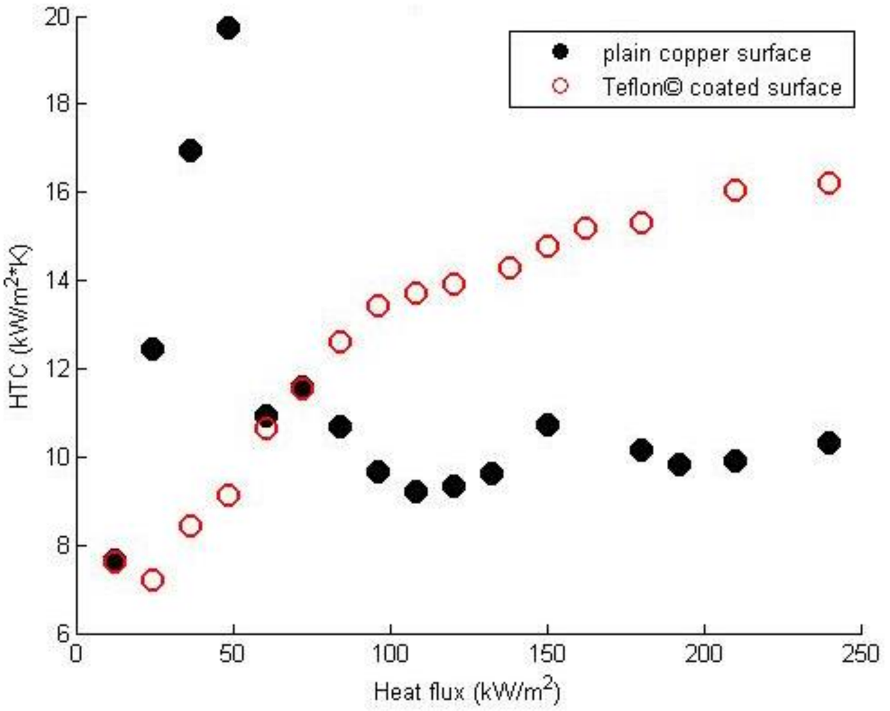

Figure 5.5 Heat transfer coefficient vs heat flux of water on Teflon coated surface and plain copper surface at atmospheric pressure

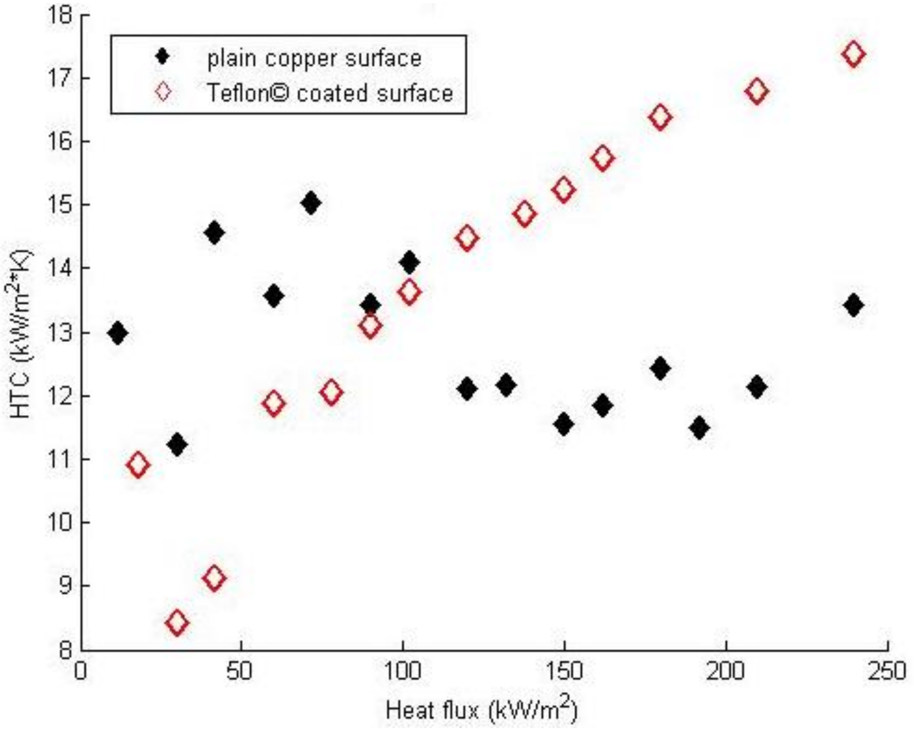

Figure 5.6 Heat transfer coefficient vs heat flux of water on Teflon coated surface and plain copper surface at 15 psig

Table 5.1 and Table 5.2 summarize the onset of nucleation for the plain copper surface and the Teflon© coated surface at different pressures respectively. For the plain copper surface, the average onset wall superheat for the bubbles is 5.2˚C at all pressures, and the average onset heat flux is 82 kW/m^2. For the Teflon© coated hydrophobic surface, the average onset wall superheat is 5.3˚C, and the onset heat flux at both pressures is 39 kW/m^2. It should be noted that at low wall superheat, due to the uncertainty of the thermocouple measurements (±2.2 ˚C), the onset wall superheat of bubbles on the two surfaces are comparable. However, bubbles do start to nucleate on the Teflon © coated surface at much lower heat flux compared to the copper surface. This indicates that due to the higher wettability of the Teflon© coated hydrophobic surface, the thermal energy that a bubble needs to form is much less than that on the plain copper surface.

Table 5.1 Onset of nucleation on plain copper surface

pressure (psig)	onset temperature (°C)	onset superheat (K)	onset heat flux(kW/m^2)
0	103.6	5.6	84
15	125.1	4.8	90
22	129.7	5.2	72

Table 5.2 Onset of nucleation on the Teflon coated surface

pressure (psig)	onset temperature (°C)	onset superheat (K)	onset heat flux(kW/m^2)
0	103.4	5.1	36
15	125.6	5.5	42

5.4 Conclusions

In this section, boiling performances of deionized water on a plain copper surface and on a Teflon© coated copper surface are investigated under atmospheric pressure and 15 psig. It was found that

- Pressure effect on heat transfer coefficient on both surfaces are higher at higher heat fluxes on both surfaces.
- Teflon© coated copper surface exhibit higher average heat transfer coefficient than the plain copper surface at both pressures.
- Energy that it takes for bubbles to form on the Teflon© coated copper surface is much less than that on a plain copper surface.

Chapter 6 - Effect of pressure on graphene oxide coated copper surfaces

6.1 Introduction

In recent years, graphene has demonstrated superb mechanical and electrical properties [57]. Graphene and graphene oxides have caught many researchers' interest in various industries. Table 6.1 is a summary of the boiling performance enhancement using graphene or graphene oxide. Although it was found that graphene and graphene oxide increased HTC and CHF, the proposed mechanisms for the enhancement are different. The two popular explanations for the enhancement in boiling heat transfer using graphene include the increased roughness of the surface, and the large thermal conductivity of graphene.

Table 6.1 Summary of boiling performance enhancement using graphene or graphene oxide

	Enhancement method	HTC Enhancement	CHF Enhancement
pool boiling	Graphene coated zirconium [58]	5%	64%
pool boiling	Graphene film [59]	90%	63%
pool boiling	Reduced GO film [60]	65%	70%
pool boiling	GO colloidal suspension [61]	N/A	63%
pool boiling	Porous graphene-deposited ITO surface [62]	186%	90%
pool boiling	Graphene-deposited ITO surface [62]	4%	9%
flow boiling	GO nano fluid [63]	N/A	20%
flow boiling	GO/water suspension [64]	N/A	100%

In this work, boiling enhancement of a graphene oxide coating on a copper substrate is compared to a plain copper surface at atmospheric pressure, 15 psig (205 kPa), 30 psig (308 kPa), and 45 psig (412 kPa) with deionized water. This is the operating pressure change for most residential boilers. Comparing the heat transfer performance at varying pressure provides additional insight into the enhancement mechanisms and makes surface coating more viable in application such as residential heating.

6.2 Surface coating

Graphene oxide is deposited on the top surface of the copper rod using spray coating. The copper rod is placed on a hot plate set at 100°C. As the copper piece is heated up, graphene oxide solution is then sprayed on to the top surface. After the solvent evaporates, the copper surface is evenly covered with a black film of graphene oxide. The sample is then baked in an oven overnight at 90°C. It is found that baking the graphene sample at a temperature lower than 90°C will decrease the adherence of the graphene coating to the copper substrate, while baking the sample at a higher temperature will make the graphene film crisp, thus prone to cracking. The thickness of the graphene oxide coating on copper substrate is measured by cutting away a small portion using a high precision micro-milling machine and visual inspecting it under a microscope. The thickness of graphene oxide varies from 2 – 9 microns as shown in Figure 6.1.

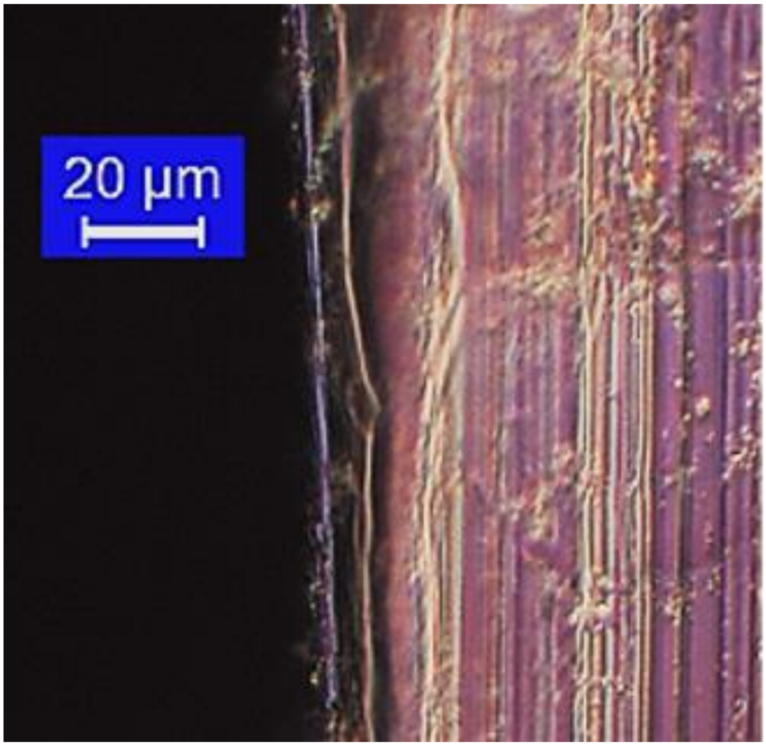

Figure 6.1 Side-view of the graphene oxide coating on the copper substrate.

Static contact angles of water on both the plain copper surface and the graphene oxide coated copper surface were measured using a static goniometer. Six contact angle measurements were taken for each surface. Figure 6.2 is a picture of one contact angle measurement on the graphene oxide coated copper surface. The average static contact angle on the graphene oxide coated surface is 80.3° with standard deviation of 2.8°, while the average static contact angle on the plain copper surface is 72.2° with standard deviation of 2.7°. Montage images are taken under a microscope at a magnification level of 2500X to examine the surface roughness of copper substrate before and after coating. The average roughness is 0.443 microns for the plain copper surface, and 0.626 microns for the graphene oxide coated surface. Figure 6.3(a-d) shows the topography and 3D image of the copper surface before and after coating.

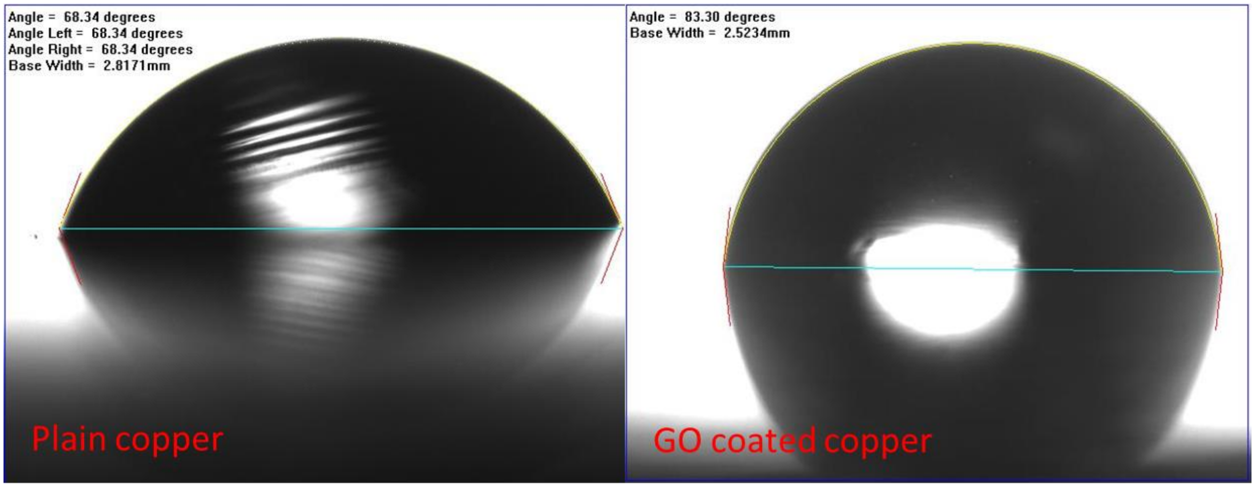

Figure 6.2 Comparison of contact angles of water on the plain copper surface and on the graphene oxide coated copper surface

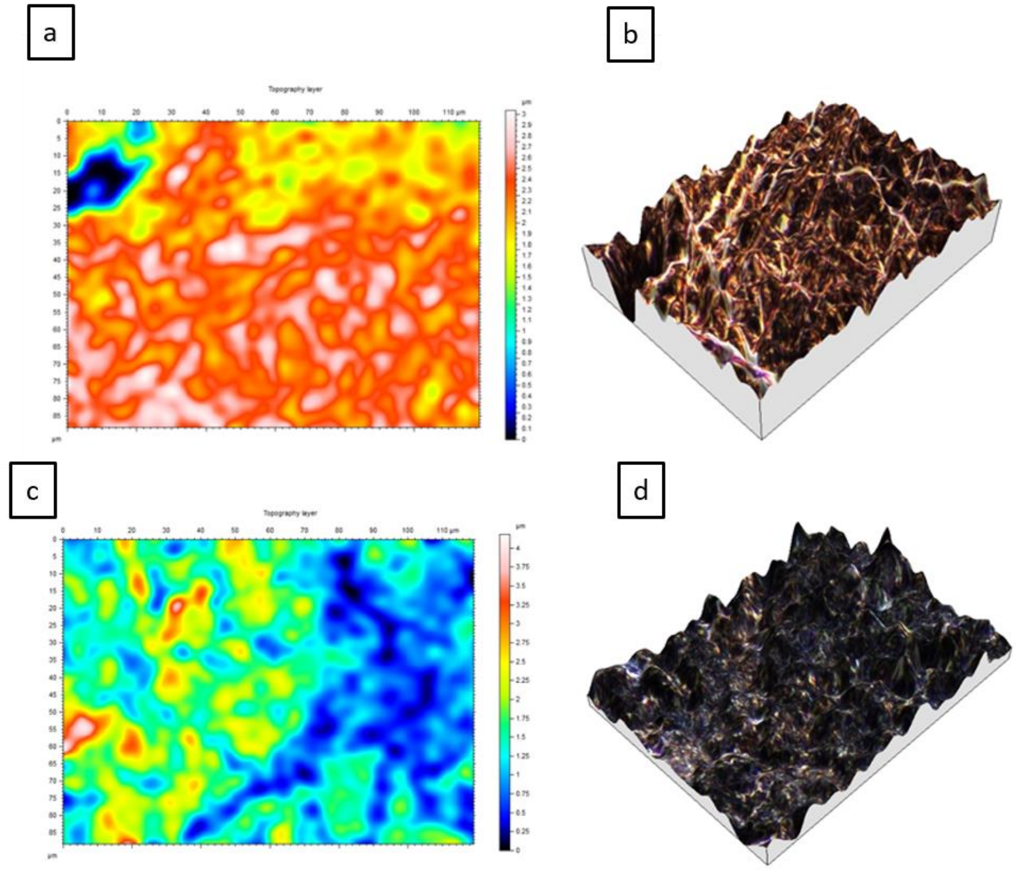

Figure 6.3 (a) Topography of plain copper surface. (b) 3D image of plain copper surface at 2500X. (c) Topography of GO coated surface. (d) 3D image of GO coated surface at 2500X.

6.3 Results and discussion

Boiling tests are conducted on a plain copper surface and on a graphene oxide coated surface from atmospheric pressure to 45 psig (412 kPa). Figure 6.4 to Figure 6.7 are the boiling curves for water on both surfaces at all pressures. When pressure increases for both surfaces, the boiling curve is shifted to the left due to the change of thermal properties of water.

At each pressure, the boiling curve of the graphene coated copper surface is always has a steeper slope than the boiling curve of the plain copper surface. However, as the pressure increases, the average distance between the two curves decreases. The dash line in each figure shows the difference in wall superheat between the two surfaces at 60 W/cm^2. This implies that at higher pressures, the heat transfer enhancement of the graphene coated copper surface is suppressed.

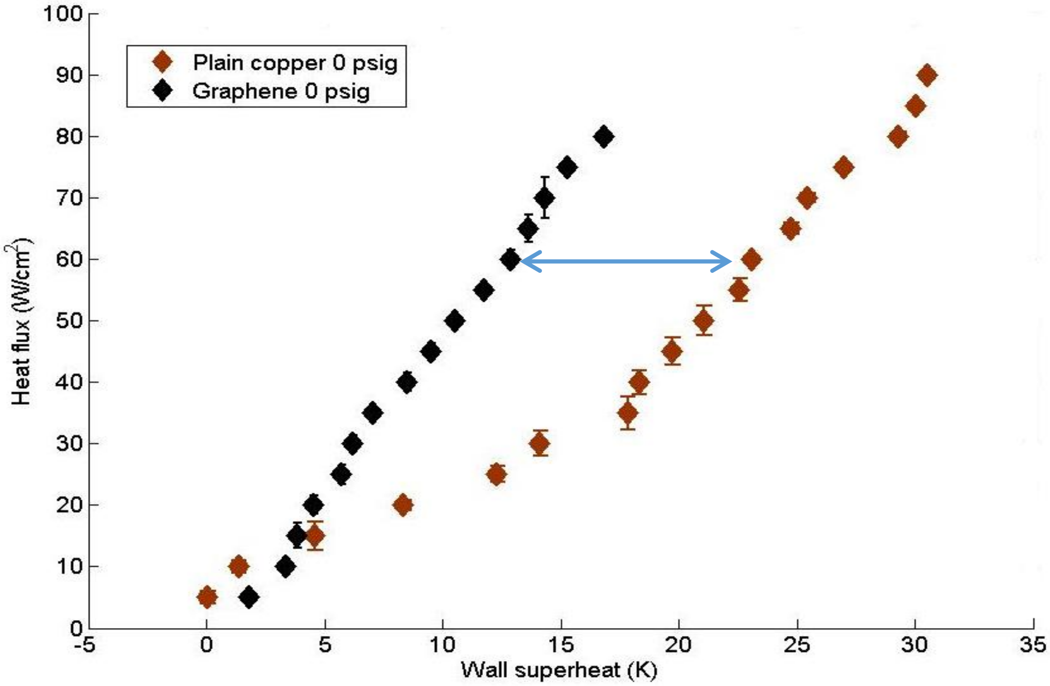

Figure 6.4 Boiling curves on both GO coated surface and plain copper surface at atmospheric pressure (0 psig)

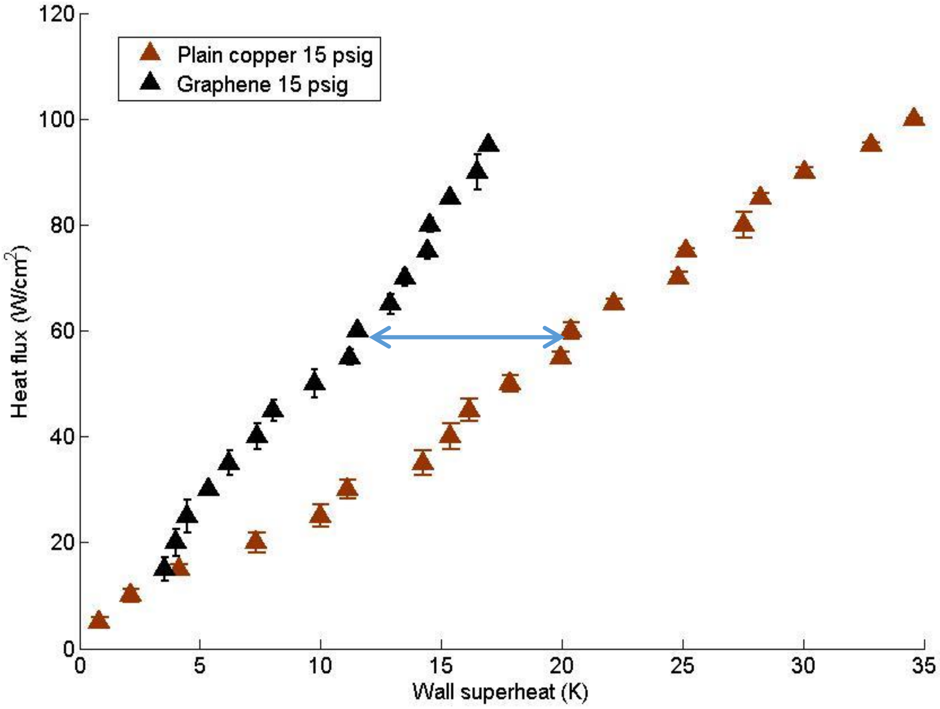

Figure 6.5 Boiling curves on both GO coated surface and plain copper surface at 15 psig

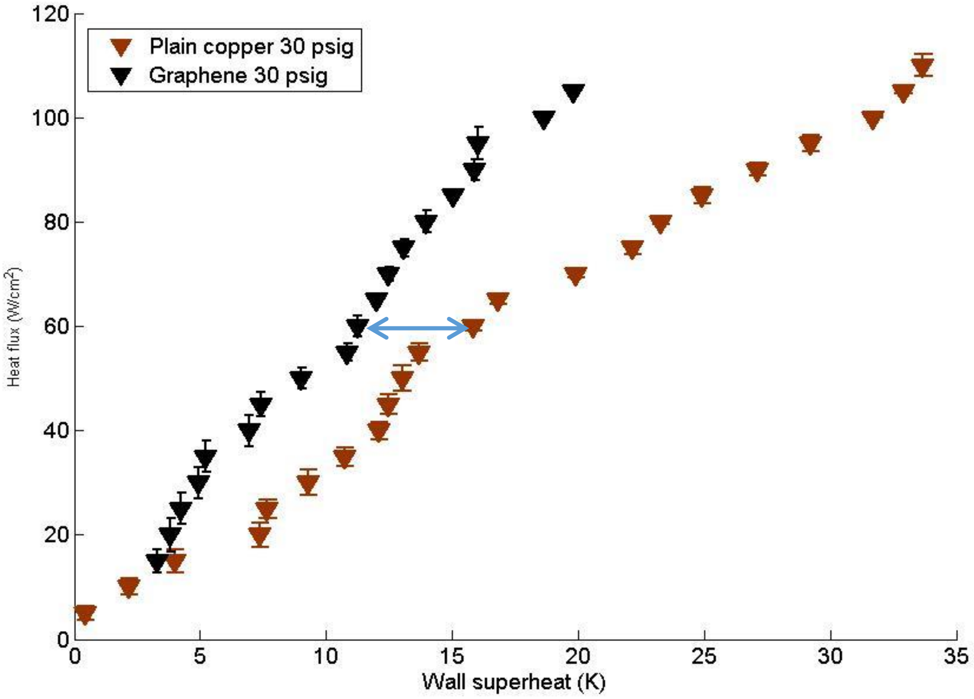

Figure 6.6 Boiling curves on both GO coated surface and plain copper surface at 30 psig

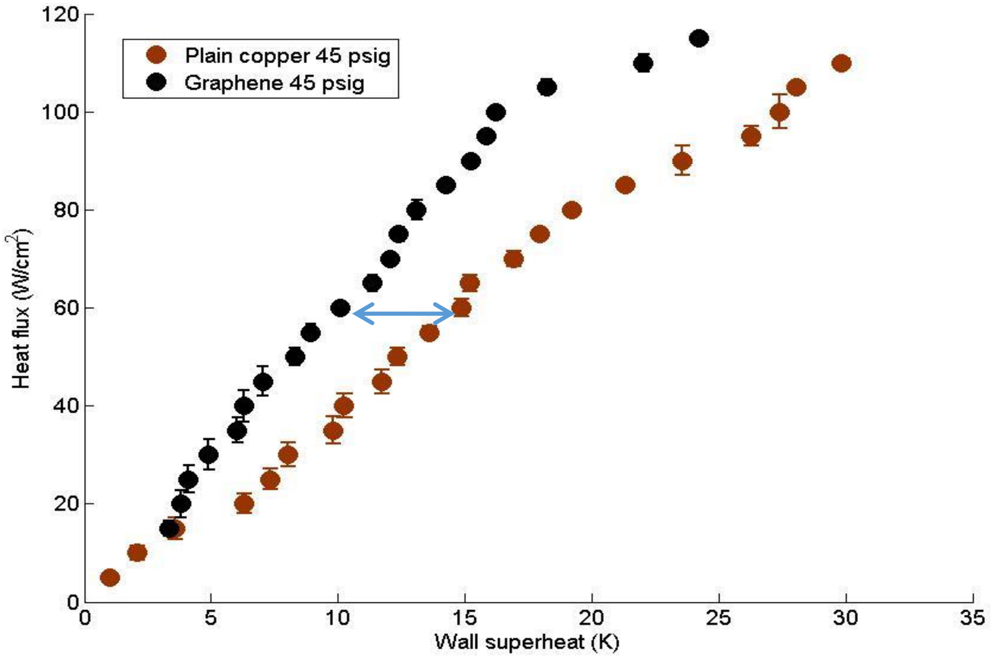

Figure 6.7 Boiling curves on both GO coated surface and plain copper surface at 45 psig

Pressure also has a positive relationship with the critical heat fluxes of the plain copper surface. Critical heat flux for the plain copper surface was found to be 85 W/cm^2 at atmospheric pressure, 100 W/cm^{2}at 15 psig (205 kPa), 110 W/cm^2 at 30 psig (308 kPa) and 45 psig (412 kPa). Critical heat flux of the graphene oxide coated surface was found to be 80 W/cm^2 at atmospheric pressure, 90 W/cm^2 at 15 psig (205 kPa), 105 W/cm2 at 30 psig (308kPa), and 115 W/cm^2 at 45 psig (412 kPa). These results demonstrate that the critical heat fluxes for both surfaces at all pressures are comparable.

The heat transfer coefficient as a function of heat flux at all pressures are plotted in Figure 6.8-Figure 6.11. Errors at low heat fluxes have a significant impact on calculated values of the heat transfer coefficient. This is mainly due to the undesired bubbles occurring at the edge around the heated surface and uncertainty from thermocouple readings at low wall superheat.

The average heat transfer coefficient of the graphene oxide coated copper surface is 43.8 kW/m^{2}K at atmospheric pressure, 52.7 kW/m^{2}K at 15 psig (205 kPa), 56.1 kW/m^{2}K at 30 psig (308 kPa), and 58.1 kW/m^{2}K at 45 psig (412 kPa). For 30 W/cm^2 heat flux, the HTC increase of the graphene oxide coated surface comparing to the plain copper surface was 126.8% at atmospheric pressure, and 51.5% at 45 psig (412 kPa).

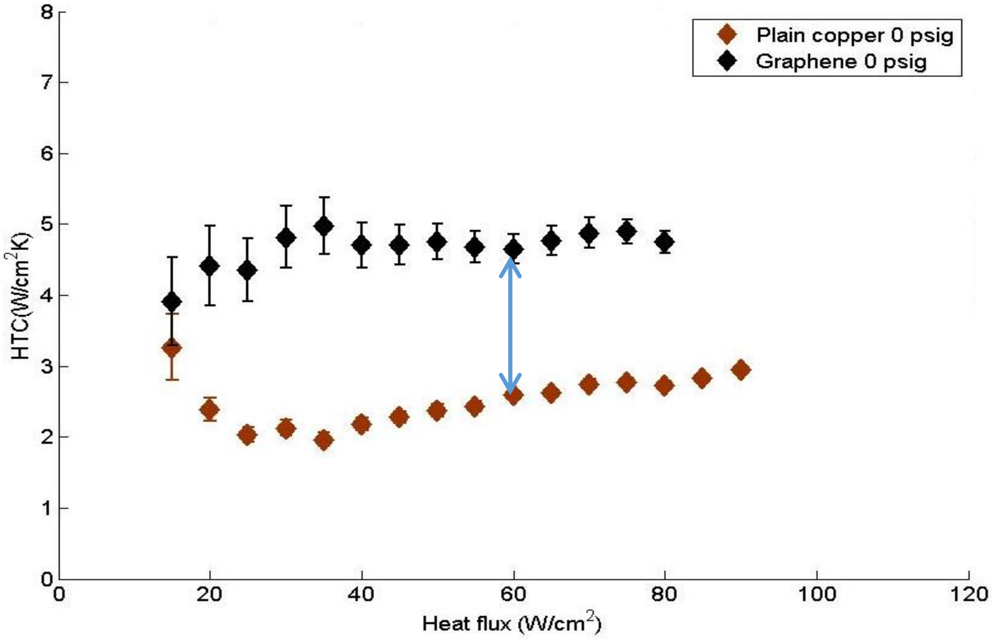

Figure 6.8 HTC vs. heat flux on GO coated surface and plain copper surface at 0 psig

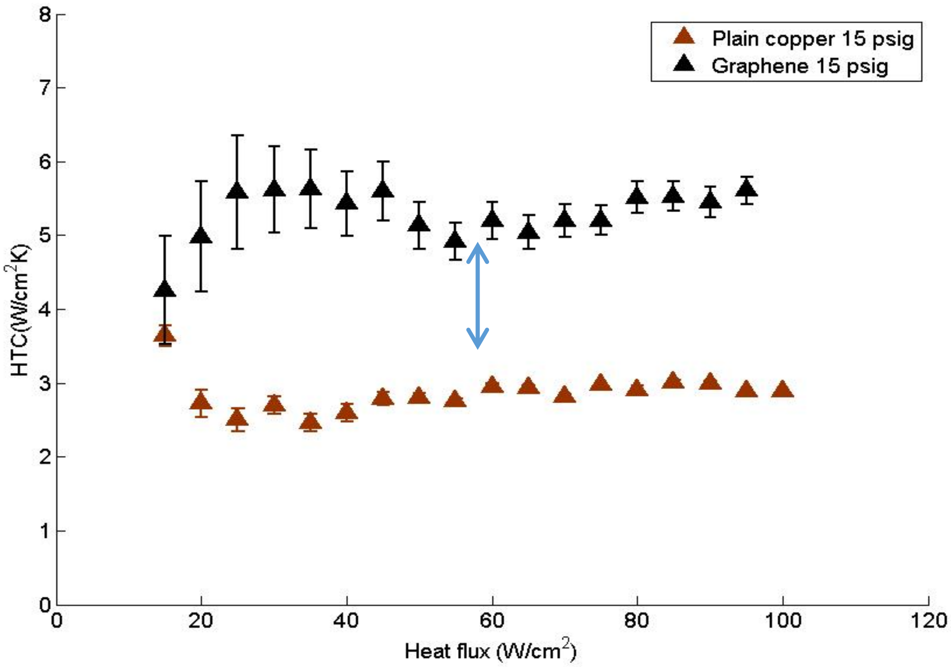

Figure 6.9 HTC vs. heat flux on GO coated surface and plain copper surface at 15 psig

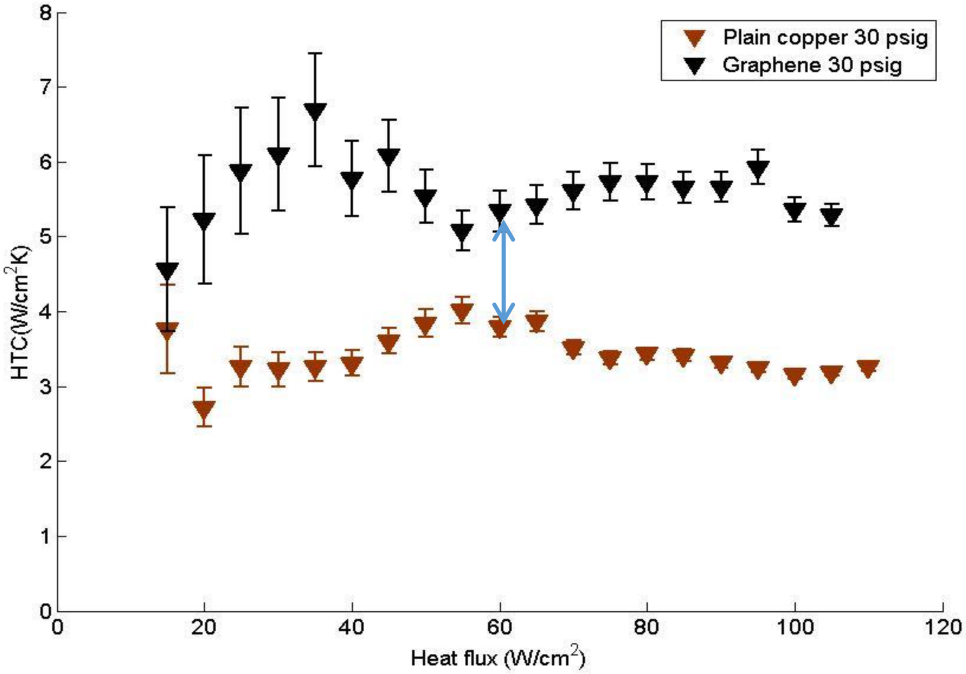

Figure 6.10 HTC vs. heat flux on GO coated surface and plain copper surface at 30 psig

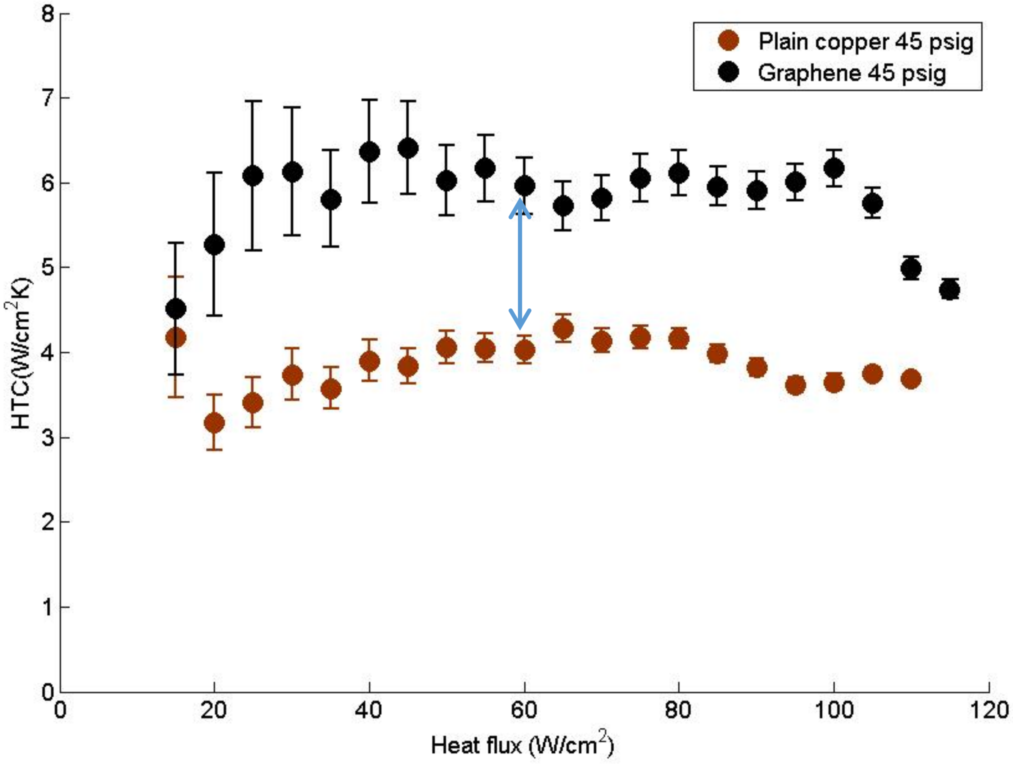

Figure 6.11 HTC vs. heat flux on GO coated surface and plain copper surface at 45 psig

Onset heat flux of bubble nucleation on the graphene oxide coated copper surface is observed to be 30 W/cm^2 at atmospheric pressure, 15 psig (205 kPa) and 30 psig (308 kPa), and 40 W/cm^2 at 45 psig (412 kPa). The onset wall superheat is found to be 6.2 K at atmospheric pressure, 5.3 K for 15 psig (205 kPa), 4.9 K for 30 psig (308 kPa), and 7.3 K for 45 psig (412 kPa). Bubble sizes on the graphene oxide coated surface are smaller compare with the plain copper surface. Figure 6.12 shows the comparison of bubble sizes on the plain copper surface and on the graphene oxide coated surface at heat flux of 30 W/cm^2 at atmospheric pressure.

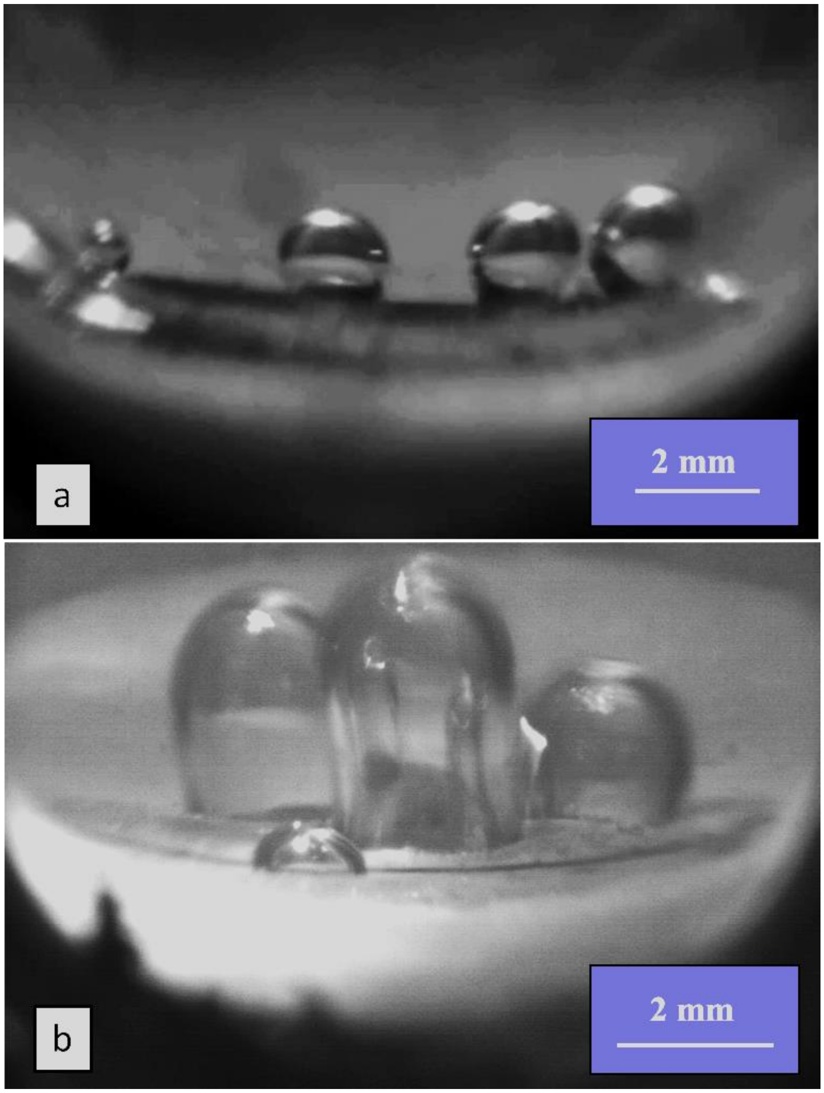

Figure 6.12 Images of bubble forming at 0 psig (101 kPa), 30 W/cm2 (a) on a GO coated surface plain copper surface (b) on a plain copper surface

On the graphene oxide coated copper surface, the HTC improvement of a graphene oxide surface change as drastically with pressure. As pressure increases, the HTC improvement of the graphene oxide coated surface decreases. As discussed in Chapter 4, HTC increases at higher pressures due to the change in the thermal properties of water. As pressures increase bubble sizes decreases, resulting in increased heat transfer coefficients. However, on the graphene coated surface, the bubble departure sizes are already smaller than on the plain copper surface. This demonstrates that the size of the bubbles are determined by the properties of the surface instead of the fluid properties. Therefore the change in thermal properties of the working fluid has less impact on the bubble departure sizes, explaining the suppressed improvement of HTC on the graphene oxide coated copper surface at higher pressures.

It is interesting to find that the graphene oxide coated copper surface has a higher heat transfer coefficient than the plain copper surface even though the contact angle of a water droplet on the graphene oxide coated surface is only slightly higher and the surface roughnesses are comparable. Also, the bubble departure diameter is significantly smaller when compared with the plain copper surface. One possible explanation for the decreased bubble diameter is that the special micro/nano structures of the graphene oxide surface created favorable nucleation sites for bubbles to grow. Due to such structures, the bubble sizes were determined by the geometry of the micro/nano structures rather than the overall wettability of the surface. Another possible explanation is that graphene actually has nonhomogeneous wettability, and the goniometer only measures the average contact angle of a water droplet on the surface. Therefore, bubbles will prefer to form on the micro/nano-scale areas that are more wetting causing the change in the size of bubbles.

Figure 6.13 is an image taken under the microscope of the graphene oxide coated surface after boiling at atmospheric pressure. It can be observed that some darker spots appear on the surface. This demonstrates that some bubbles were pinned on the surface during the boiling process and redeposition of graphene occurred.

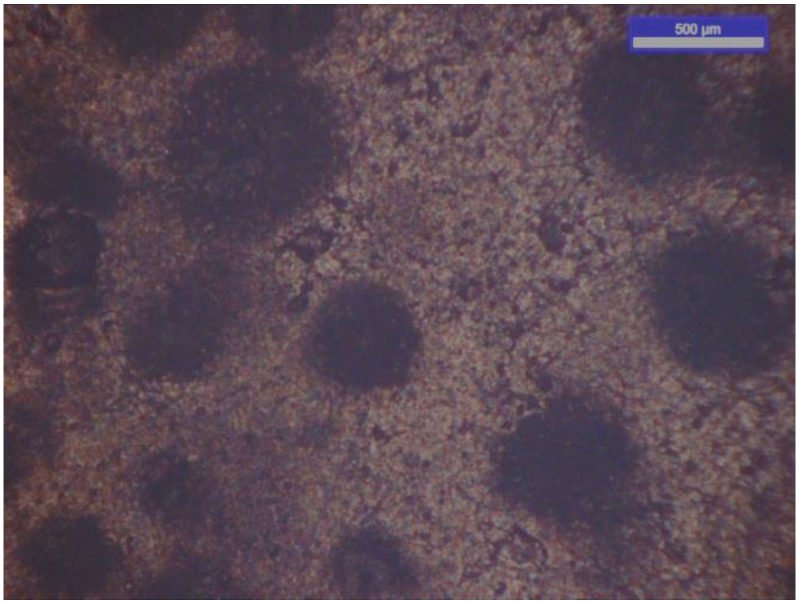

Figure 6.13 Image of the graphene oxide coated surface after boiling

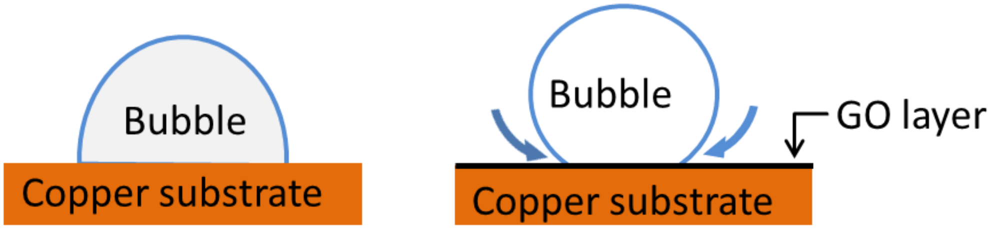

Figure 6.14 Pinning of bubble provides liquid pathway for rewetting the surface

The decreased bubble size on the graphene oxide coating allows more bubble nucleation sites on the surface. As a result, more heat could be removed from the heated surface, making the heat transfer coefficient higher for the coated surface. At higher heat fluxes, the violent bubble formation and merging diminished the effect of bubbles pinning on micro/nano structures or nonhomogeneous wettability, and the macroscopic property (i.e. wettability) of the graphene oxide coating started to dominate. Since the wettability of the plain copper surface and the graphene oxide coated surface is similar, the critical heat fluxes on both the surfaces are comparable.

6.4 Conclusions

In this chapter, nucleate pool boiling performance of deionized water on a graphene oxide coated surface and a plain copper surface at varied pressures from atmospheric pressure up to 45 psig (412 kPa) were investigated. It was found that:

- Heat transfer coefficient increases as the pressure increases for both surfaces. The graphene oxide coated surface has a higher heat transfer coefficient than the plain copper surface at the same pressure, although the heat transfer enhancement diminishes as the pressure is increased.
- Bubble sizes on the graphene oxide coated surface are observed to be significantly smaller than those on the plain copper surface. These characteristics could be due to the pinning effect of bubbles by the micro/nano structures on the graphene oxide surface, and/or the nonhomogeneous wettability of the graphene oxide surface.
- The pinning effect of bubbles will diminish at higher heat fluxes, and the macroscopic property of the graphene oxide coated surface will dominate the heat transfer behavior on the graphene oxide copper surface.

Chapter 7 - Characterization of engineered surfaces

7.1 Overview

In order to further understand the micro/nano or nonhomogeneous wettability of the engineered surface, condensation experiments were conducted on a graphene coated copper surface, and freezing experiments were conducted on nanoporous structured silicon surfaces. Condensation and freezing behaviors on these engineered surfaces are drastically different. Pinning of water droplets were also found on these surfaces. The freezing experiment on the nanoporous surfaces also demonstrates that the pinning droplets affects the freezing dynamics, resulting in reduced freezing time.

7.2 Experimental apparatus

Freezing and condensation on engineered surfaces experiments are conducted in a freezing stage in a computer controlled environmental chamber at the Kansas State University Institute of Environmental Research under quiescent flow conditions with a controlled relative humidity (RH) and an initial constant air temperature of 295 K. The relative humidity and temperature of the chamber were also independently verified using an Omega RHXL3SD thermometer/hygrometer. The freezing stage, depicted in Figure 7.1, was composed of Peltier cooler connected to a TE Technologies TC-720 temperature controller and MP-3176 thermistor. The hot side temperature was maintained by an aluminum heat sink supplied with ice water from a Fisher Scientific FH100D peristaltic pump. The stage temperature was independently monitored by a thin film Omega thermocouple connected to a National Instruments data acquisition system (DAQ-9174 with NI 9211 module). Chamber relative humidity varied between 30 – 60 % RH. Videos were captured by a Leica DVM2500.

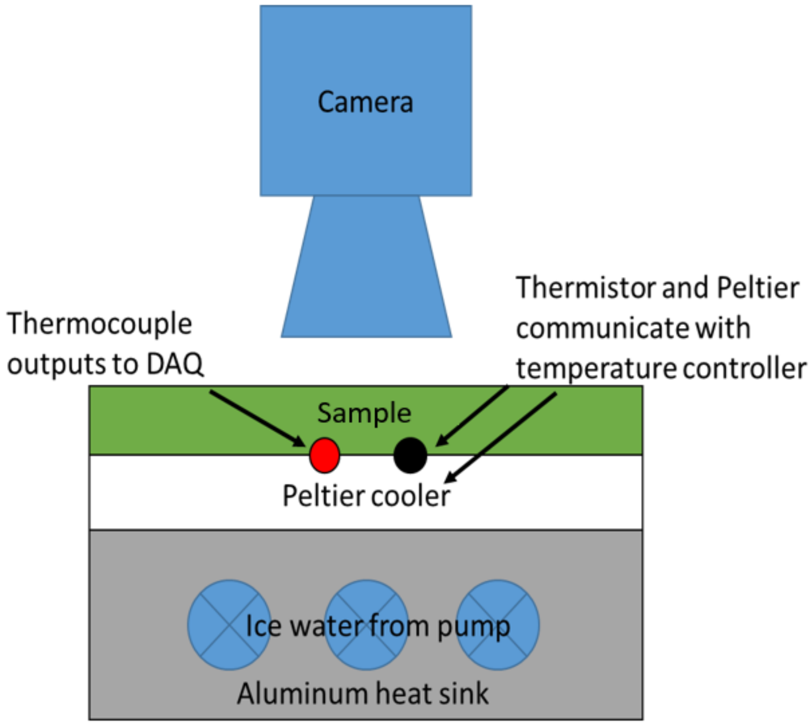

Figure 7.1 Schematic of the freezing stage

7.3 Condensation over graphene coated copper surface

7.3.1 Overview

Condensation experiments were conducted on a plain copper surface and a graphene oxide coated copper surface to further demonstrate that the micro/nano structures or the nonhomogeneous wettability of the graphene oxide plays a huge role in the two phase heat transfer process. The copper substrates are 25.4 mm in diameter and 3 mm in thickness. Both samples were manufactured with the same process as the samples used in the boiling experiments. The samples were placed on the freezing stage in the environmental chamber where the temperature was controlled at 22˚C and the relative humidity at 40%. The surface was cooled with a Peltier cooler at 4°C. A microscope recorded the condensation process on each surface at 1 frame per second.

7.3.2 Results and discussion

Condensed water droplet formation on both surfaces was observed under a microscope, as shown in Figure 7.2 and Figure 7.3. It is found that on the plain copper surface, the condensed water droplets evenly distributed all over the surface and had uniform round shapes. During the condensation process on the plain copper surface, the water droplet sizes over the entire surface were uniform. As the water droplets grew, the neighboring droplets coalesced with each other forming a larger round shaped droplet. Furthermore, coalescence moved the droplets, creating dynamic interactions on the cleared surface. Droplet coalescence and direct condensation both contribute to the growth of the droplets on the plain copper surface.

On the other hand, for the graphene oxide copper surface, some of the condensed water droplets are pinned to random spots over the surface. As the droplets grew and coalesce, due to the pinning effect, the merged droplets form non-spherical irregularly shapes as shown in Figure 7.3. The size difference of the droplets on the graphene coated copper surface are more apparent than on the plain copper surface. The growth of the droplets on the graphene coated copper surface are mainly due to coalescence. The growth rate by direct condensation is lower on the graphene coated copper surface than on the plain copper surface. The irregular shape of condensed water droplets on the graphene coated surface suggests that the existence of micro/nano structure or nonhomogeneus wettability of the graphene coated surface.

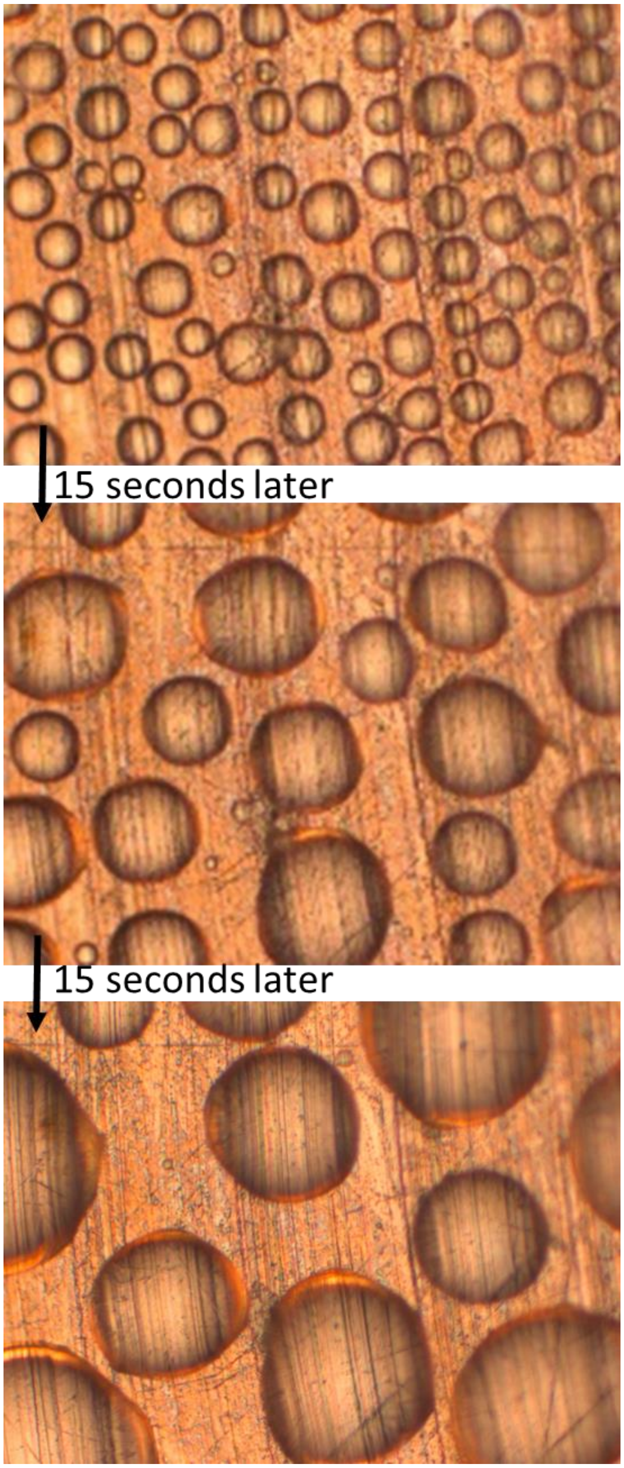

Figure 7.2 Condensed water droplets on plain copper surface (dimension 612 x 459 µm)

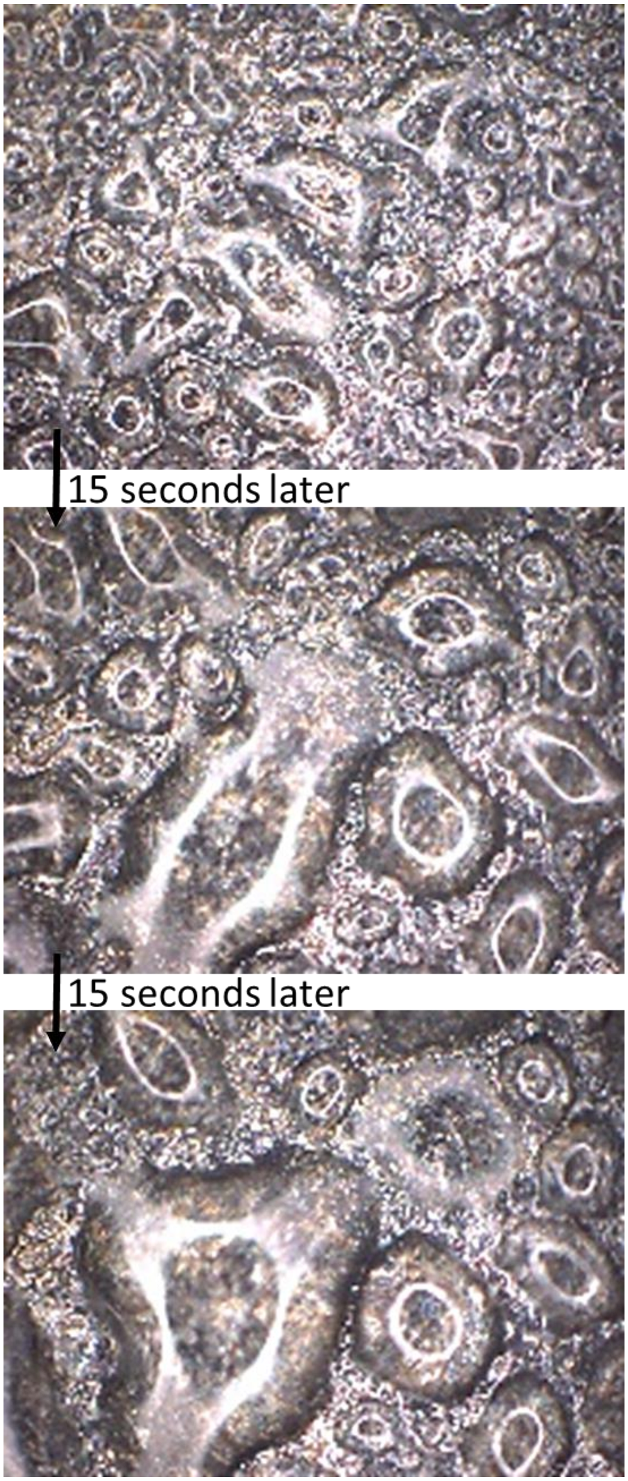

Figure 7.3 Condensed water droplets on graphene oxide coated surface (dimension 612 x 459 µm)

7.4 Frost formation on nanoporous hydrophilic surfaces

Water droplet nucleation, coalescence, and subsequent freezing were studied on nanoporous surfaces and hydrophilic silicon oxide surfaces. In order to achieve freezing, samples were placed in an environmental chamber with surface temperatures of 265 K. Videos were taken with a microscope at 100 frames per second.

7.4.1 Fabrication of nanoporous and hydrophilic surfaces

Nanoporous surfaces were fabricated using Microsphere Photolithography (MPL), which is a low-cost, bottom-up fabrication technique [65] . The process begins with arrays of self-assembled microspheres on the substrate, forming a hexagonal close packed (HCP) crystal. This process is depicted in Figure 7.4. For the nanoporous surfaces utilized in this study, HDMS adhesion promoter was applied to a polished silicon wafer. Positive tone photoresist, S1805 (Shipley), was spin-coated to a thickness of 480 nm ± 20 nm. Following soft-baking of the resist at 115°C, a microsphere solution consisting of 2 µm diameter polystyrene spheres (Polysciences) dispersed in water (8.9% wt.) was drop coated onto the photoresist. As the water evaporated, the microspheres self-assembled. At the conclusion of this process, the entire sample was flood illuminated using an i-line mask aligner (MA6, Karl Suss). After exposure, the sample was hard-baked at 145°C before developing in MF319 (Rohm Haas). During development the microspheres were removed from the substrate to reveal the nanopores with diameters of 500 – 750 nm, depending on the exposure time.

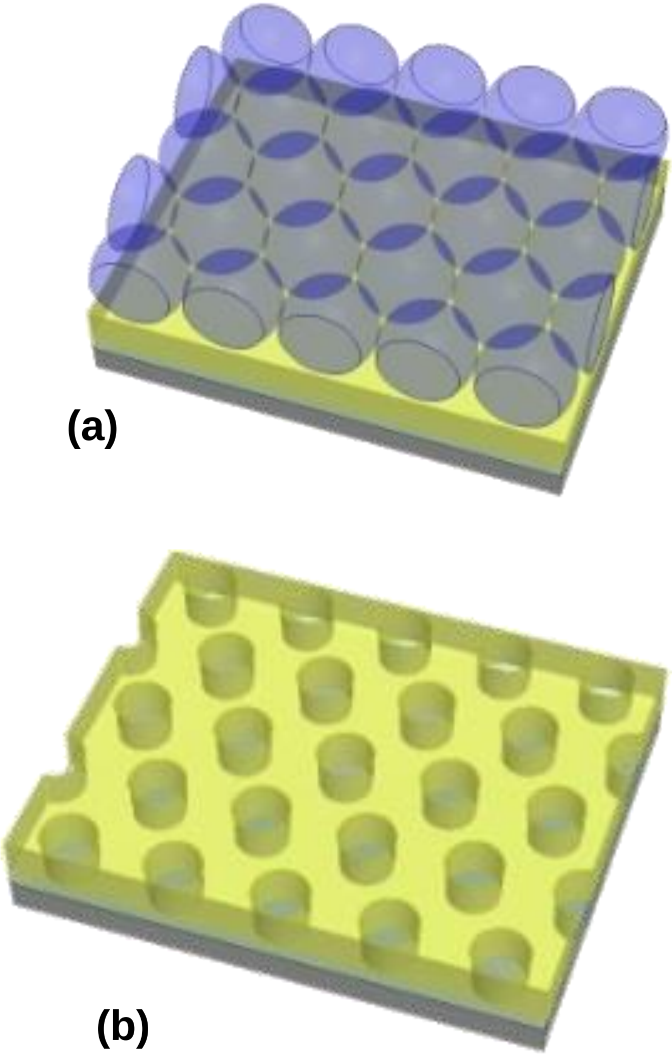

Figure 7.4. Microsphere Photolithography process showing (a) microspheres self-assembled on photoresist surface, (b) pattern after exposure and development

7.4.2 Results and discussion

As the surface cooled, droplets began to condense on the surface. For the plain silicon oxide surface, droplets grew and some merged or coalesced, as shown in Figure 7.5. Droplet growth by direct condensation is slow. In Figure 7.5, the circled droplet growing by direct condensation increased in diameter by only 25% after two minutes. Whereas, in the locations were coalescence had occurred, the droplet diameter greatly increased. Increased coalescence leads to an increase in freezing time due to a combination of dynamic droplets, increased droplet size, and surface energy reduction.

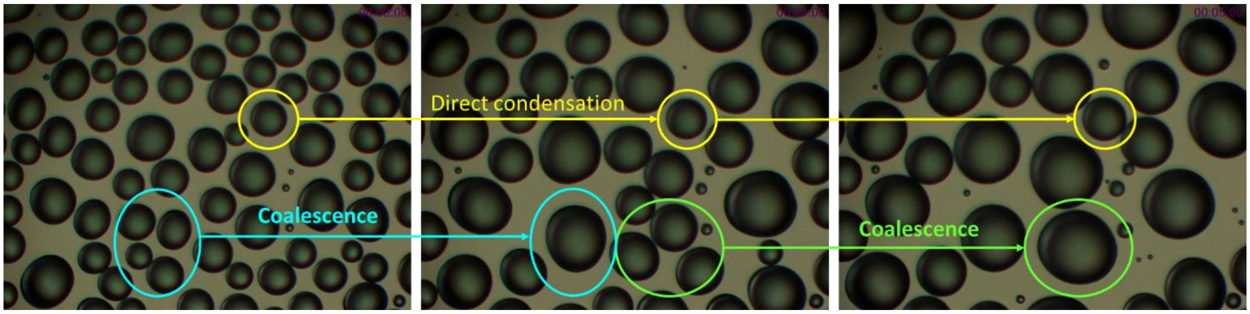

Figure 7.5. A time-lapsed image sequence of condensation on the silicon oxide surface at 40% relative humidity elucidates the rate of droplet growth through direct condensation compared to coalescence. The time between frames is 1 minute and each image is 765 × 574 µm.

In contrast, the nanopores on the patterned surface pinned the droplets, preventing them from fully coalescing and creating non-spherical droplets, shown in Figure 7.6. Droplets continued to grow through direct condensation, but the direct growth process was slow compared to coalescence and the droplets froze just minutes after the condensation process began.

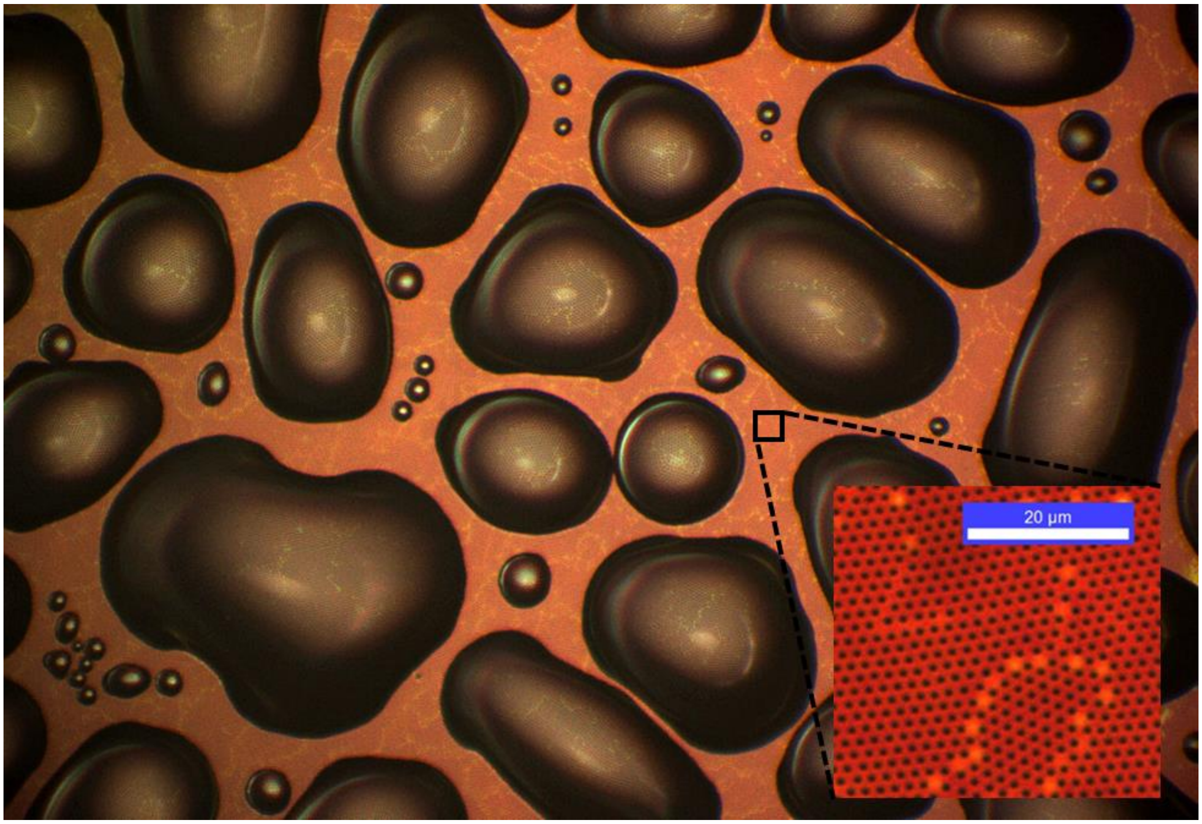

Figure 7.6. Droplet pinning on the nanoporous surface and close-up of the nanoporous surface (inset)

The nanoporous surfaces had decreased freezing times (defined as the time required for the entire surface to freeze) at relative humidities ranging from 30–60%, as shown in Figure 7.7. Each surface was tested at least three times at each relative humidity with a constant air temperature of 295 K. Because freezing time was determined through visual inspection, the uncertainty for the freezing time was conservatively estimated to be ± 2 minutes. Different freezing behavior was apparent on the different surfaces; freezing times for the nanoporous surfaces were around 4–5 minutes, while freezing time was a strong function of relative humidity for the silicon oxide surfaces. The greatest difference in freezing time occurred at 30% RH; the nanoporous surface froze in 5 minutes, compared to 19 minutes for the silicon oxide surface. At this lower relative humidity, there is less available moisture in the air and droplet coalescence on the silicon oxide surface prolongs freezing. In contrast, at higher humidities, the rate of droplet growth due to direct condensation is greater and less coalescence is necessary for the entire surface to freeze. At 60% RH, the change in the average freezing time between the surfaces was negligible. This is consistent with previous work which demonstrated that 60% RH was the shortest freezing time for silicon oxide surfaces [68]. The droplet pinning on the nanoporous surface does not completely prevent droplet growth or merging since droplets continue to grow due to direct condensation at the droplet interface. The time required for the nanoporous surface to freeze remains relatively constant regardless of relative humidity due to the suppression of droplet coalescence.

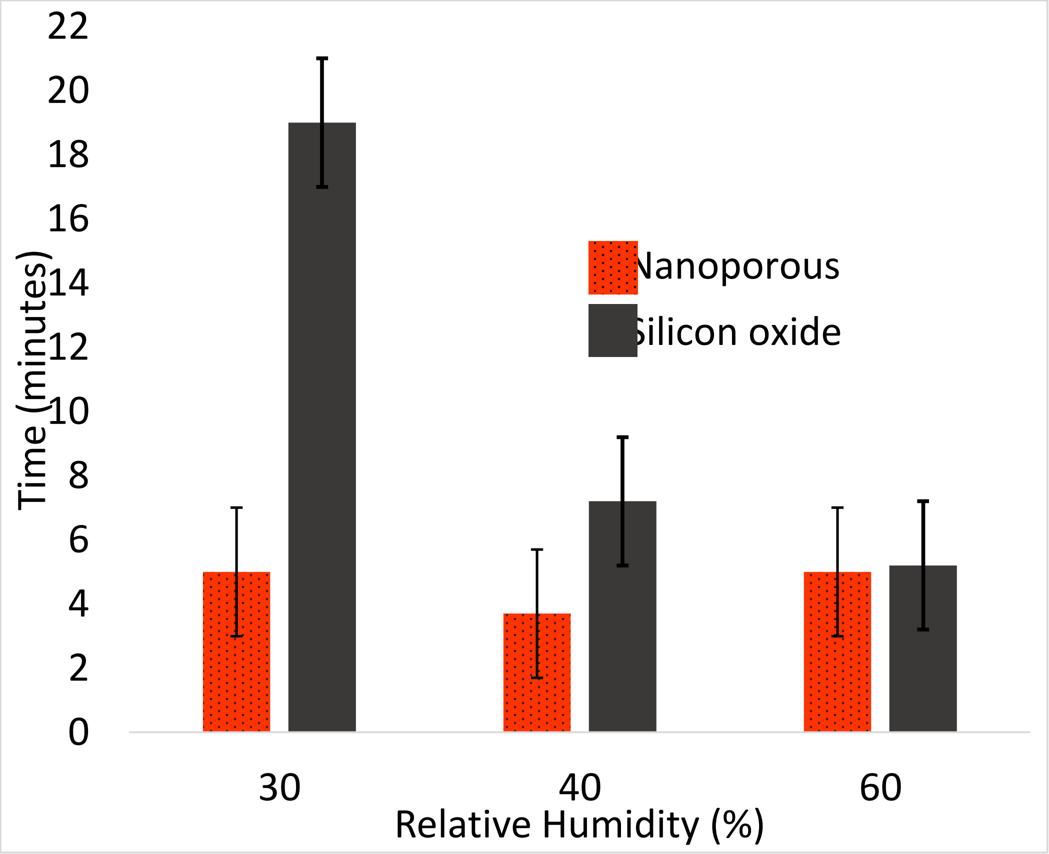

Figure 7.7. Freezing time for the nanoporous surface compared to the silicon oxide wafer at 30%, 40%, and 60% relative humidity.

It is hypothesized that the unusual, non-spherical droplet shapes observed on the nanoporous surface are a result of the droplets being pinned in the nanopores, thereby affecting freezing behavior (Figure 7.6). Nanopore dimensions needed to be in an optimal range to pin the droplets. In order for the holes to prevent coalescence, the energy required to overcome the capillary pressure (Ecap) must be greater than the surface energy reduction by coalescing droplets, Eq. 7.1.

$$\mathrm{Ecap} \geq \mathrm{SAred} \qquad \text{Eq. 7.1}$$

The total energy required to overcome the capillary pressure will be the capillary pressure (Pcap) is,

$$\mathrm{Ecap} = \mathrm{Pcap} \cdot V \cdot n\text{\`{}} \cdot \mathrm{Ac} \qquad \text{Eq. 7.2}$$

where V is water volume in a pore, n` is pore density, and Ac is the contact area of a drop. The surface area reduction from two coalescing droplets assumes that the droplets are spherical caps and that the two coalescing droplets have the same radius (Rd1). With these two assumptions, the reduction in surface energy depends on the contact angle (θ) and the droplet radius, Eq. 7.3. It should also be noted that a contact angle less than 90° is required.

$$\mathrm{SAred} = 2^{1/3}\pi \cdot (\mathrm{Rd1})^2 \cdot (1+((1-\cos\theta)/\sin\theta)^2) \qquad \text{Eq. 7.3}$$

Substituting in parameters for the equations above, the capillary energy depends on the surface tension of water in air (σ), the radius of the pores (r), the depth of the pores (δ), and the density of the pores, Eq. 7.4.

$$4\pi \cdot \sigma \cdot \cos\theta \cdot r \cdot \delta \cdot n\text{\`{}} \geq 2^{1/3}(1+((1-\cos\theta)/\sin\theta)^2) \qquad \text{Eq. 7.4}$$

The pore density is assumed to be a function of the pore radius with a pitch of 4r, Eq. 7.5. The pores on the actual surface are arranged in a more densely packed staggered arrangement, see Figure 7.6. However, due to dislocations and grain boundaries in the nanoporous structure, the actual pore density is difficult to determine for any given droplet. The pore density used in the calculations provides a conservative estimate,

$$n` = 1/(16r^2) \qquad \text{Eq. 7.5}$$

Equation 7.4 can be simplified and the required pore radius is a function of surface tension (σ), the contact angle (θ), and the depth of the pores (δ), Eq. 7.6.

$$r \geq [(1/4)\pi\cdot\sigma\cdot\cos\theta\cdot\delta]/ \{2^{1/3}(1+[(1-\cos\theta)/\sin\theta]^2)\} \qquad \text{Eq. 7.6}$$

There is a suitable pore size range which will exhibit this droplet pinning behavior. The pore diameter should be in the range of active nucleation site size to ensure that the water condenses in the interior of the hole [69], and the pore diameter should be smaller than the initial nuclei so that water fills the hole and the droplets span multiple holes and capillary pressure is significant. According to Leach et al.[69], active nucleation site sizes range from 100 nm – 30 μm depending on conditions and initial water nuclei are typically around 1 - 10 μm in size. This sets the limit of possible pore diameters between 100 nm – 10 μm, Figure 7.8. Assuming water as the fluid condensing on the surface, Figure 7.8 provides the diameter required to pin the droplets, reduce coalescence, and accelerate freezing. The dashed circle on the graph represents the contact angle and pore sizes investigated in this work.

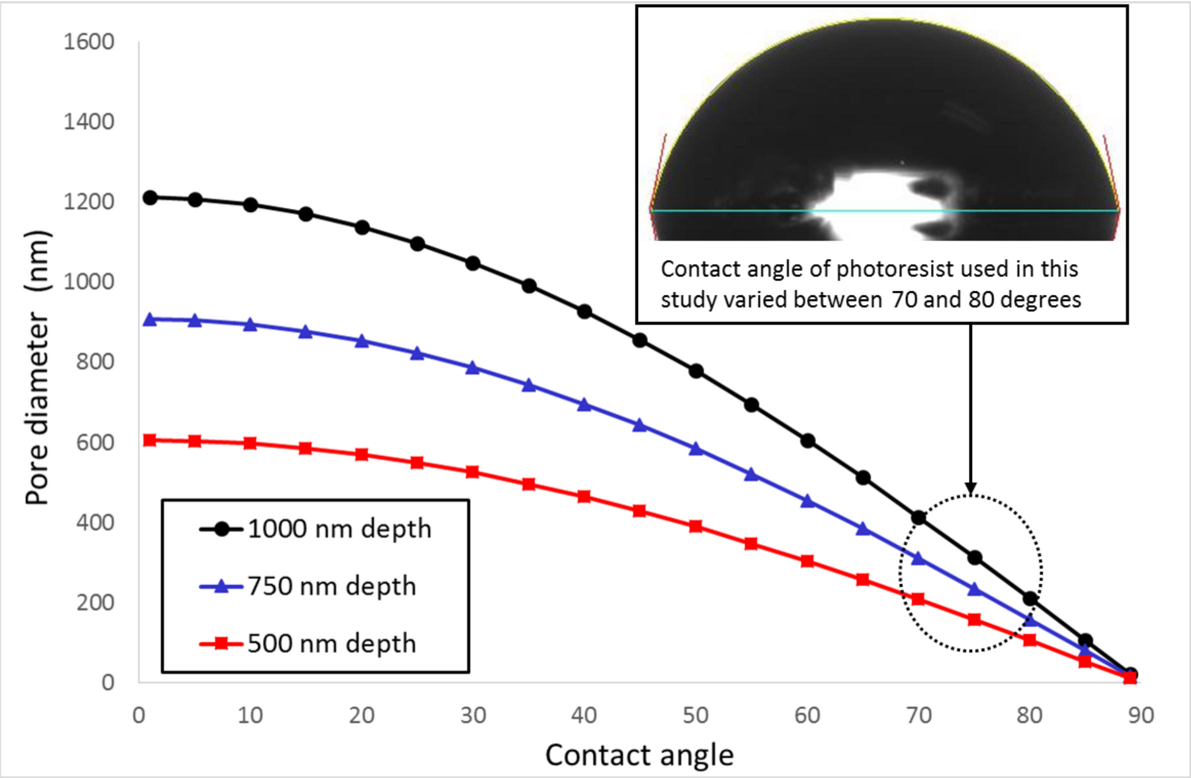

Figure 7.8. Modeled pore diameter required for the energy to overcome the capillary pressure to equal the energy reduction from coalescence at varying contact angles and pore depth. The region of contact angle and pore diameters studied are shown with a dashed line.

Droplet pinning altered the freezing time and changed the structure of ice on the surface. On the hydrophilic silicon oxide surface, there was a clear freezing front propagation, and ice bridging was observed as the main mechanism for the freezing front propagation [70], as shown in Figure 7.9. On the nanoporous surface, the freezing front was more challenging to track because freezing was more rapid. During several tests, all the droplets in the field of view froze in a single frame (0.01 seconds), or a random pattern of freezing was observed. At 40% RH, the freezing front propagation on the silicon oxide surface was 0.73 mm/min and propagated from the upper right corner of the frame to the lower left corner. The propagation rate was determined by dividing the diagonal length of the frame by the total time required for every droplet in the frame to freeze. The freezing front propagation was limited by the growth rate of the ice bridging crystals particularly on the silicon dioxide surface, Figure 7.9. Observed ice bridge crystals grew at an average rate of 0.11 mm/min with a standard deviation of 0.029 mm/min. This growth rate is consistent with, albeit slightly higher than, previously reported data [73]. The freezing front can propagate faster than the crystal growth because droplet freezing also contributes to the freezing front propagation. On the nanoporous sample at 40% RH, the freezing front was distinguishable and the propagation rate was much higher, 5.2 mm/min. When drops froze on the nanoporous surfaces, there was very little change in the index of refraction or reflectance so that the patterns beneath the drops were visible through the ice nuclei, see Figure 7.9.

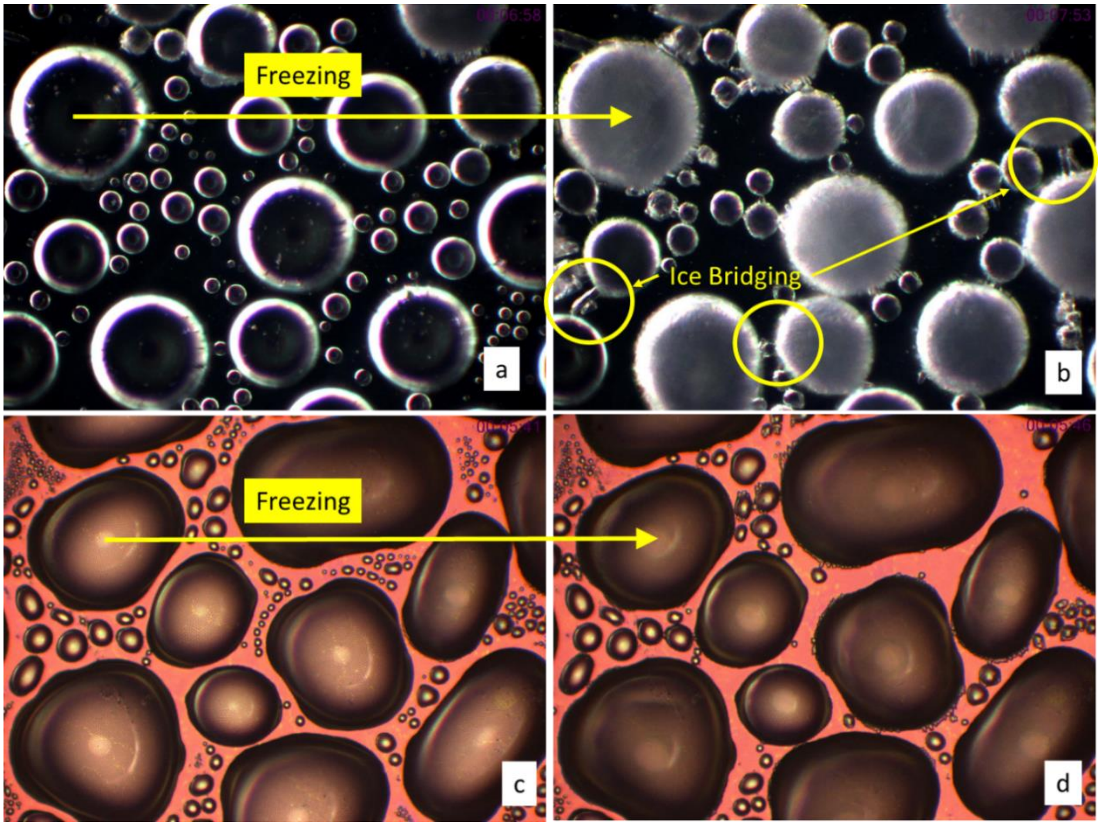

Figure 7.9. Droplets on the silicon oxide surface (a) before and (b) after freezing compared to the nanoporous surface (c) before and (d) after freezing at 40% relative humidity. Surfaces were maintained at 265 K and the images are 765 × 574 µm.

7.4 Conclusions

Micro/nano structures or nonhomogeneous wettabilities have profound impact on freezing and condensation behaviors. Graphene oxide coated copper surface has random micro/nano structures, while the nanoporous surface has regularly arrayed nanostructure. It was found that the pinning of droplets occurs on micro/nano structured or nonhomogeneous wettability surfaces. Due to the pinning effect, condensation and freezing dynamics were changed. Without pinning, droplets move during coalescence creating dynamic interaction with the surface. Freezing experiments further demonstrates that the nanoporous surface changed the freezing behavior of droplets. This implies that pinning of vapor bubbles on graphene oxide coated surface plays a huge role in affecting the bubble dynamics, thus enhancing the boiling performance.

Figure 7.10 (a) Redeposition of graphene of bubbles pinning on the graphene oxide coated surface, (b) droplets pinning on the graphene oxide coated surface, (c) droplets pinning on the nanoporous surface

Chapter 8 - Conclusions and future work

8.1 Conclusions

The boiling performance of deionized water at various pressures (from atmospheric pressure to 45 psig) was experimentally examined on a plain copper surface, a Teflon© coated copper surface, and a graphene coated copper surface. To further understand the physical insights of engineered surfaces, condensation experiments were conducted on graphene coated copper surfaces, and freezing experiments were conducted on nano-structured silicon surfaces

- Effect of pressure

Test results show that elevated pressures increase both the heat transfer coefficient (HTC) and critical heat flux (CHF) of water. Onset of bubble nucleation was delayed at higher pressures. Increased pressure also decreases the bubble sizes. The rate of increase in heat transfer coefficient due to pressure on different surfaces are not the same due to the different surface properties. The effect of pressure on the graphene coated surface was suppressed. The enhancement of the boiling performance at elevated pressure is due to the change in the thermal properties of water at higher pressures.

- Effect of engineered surfaces

Engineered surfaces have huge effect on the boiling performances of water. Experimental results on the Teflon© coated copper surface manifests that hydrophobic surfaces have higher heat transfer coefficient. Onset of nucleation occurs at smaller heat fluxes on the hydrophobic surfaces at both pressures. At the same pressure, bubble sizes were found to be larger on the hydrophobic surfaces than those on the plain surfaces. Since the hydrophobic surface has less surface energy, the energy required for bubbles to form on the hydrophobic surface is decreased. Therefore the heat transfer rate is enhanced on the hydrophobic surfaces.

On the graphene coated surface, the heat transfer coefficient was greatly enhanced but the critical heat flux remained similar compared with the plain copper surface. Although the plain copper surface has higher wettability than the graphene coated surface, the bubble sizes on the graphene coated copper surface are found to be significantly smaller than the plain copper surface. Pinning effect of bubble observed during the boiling process. It is postulated that the pinning effect of bubbles occurs because of the micro-nano structure, and/ or the nonhomogeneous wettability of the graphene coated surface. At higher heat fluxes, the effect of microscopic properties of the surfaces diminish and the effect of the macroscopic property of the surface start to dominate, explaining the similar critical heat fluxes on both surfaces at each pressure.

- Physical insights on engineered surfaces.

Both the condensation experiments on the graphene coated copper surface and the freezing experiments on the nanoporous silicon surface show that the micro/nano structure of the surfaces have a huge impact on the bubble dynamics. Water droplets on the engineered surfaces have irregular shapes due to the pinning effect, which greatly impacts the condensation and freezing behaviors of water. The results imply that the pinning of bubbles on the graphene coated surface affects the heat transfer performance in boiling processes.

8.2 Future work

In order to further understand the effect of pressure on engineered surfaces, more boiling experiment will be done on engineered surfaces at higher pressures. Since the rate of increase in the heat transfer coefficient is smaller on the engineered surfaces than on the plain copper surface, there should be a pressure at which engineered surfaces have little impact on the boiling heat transfer.

In this work, the graphene coated copper surface has randomly patterned mico/nano structure, and randomly patterned nonhomogeneous wettability. In order to explore how pinning effect of bubbles affects the bubble dynamics, the next step is to design and manufacture regularly patterned biphilic surfaces, and examine the bubble formation on these surfaces in boiling tests. The effect of the newly designed engineered surfaces on the boiling performance of water will also be studied at different pressures. Numerical models will be developed for the regularly patterned engineered surfaces. Condensation and freezing behavior of the engineered surface will also be examined.

References

[1] Dhir, V.K., 1988, “Boiling Heat Transfer,” vol. 30, PP. 365- 401.

[2] R.L. Webb, “Donald Q. Kern Lecture Award Paper: Odyssey of the Enhanced Boiling Surface,” Journal of Heat Transfer, Vol. 126, Dec. 2004, pp. 1051-1059.

[3] Theofanous, T. G., T. N. Dinh, J. P. Tu, and A. T. Dinh. 2002. "The Boiling Crisis Phenomenon Part II: Dryout Dynamics and Burnout." Experimental Thermal and Fluid Science 26 (6-7): 793-810. doi:10.1016/S0894-1777(02)00193-0.

[4] Westwater, .I. W., Santangelo, J. G., IND. END. CHEM. 47, 1605 (1955).

[5] Y.Y. Hsu, On the Size Range of Active Nucleation Cavities on a Heating Surface, Journal of Heat Transfer, 207-216 (1962).

[6] Buongiorno, J., L. W. Hu, G. Apostolakis, R. Hannink, T. Lucas, and A. Chupin. 2009. A feasibility assessment of the use of nanofluids to enhance the in-vessel retention capability in light-water reactors. Nuclear Engineering and Design 239 (5) (5): 941-8.

[7] Di Marco, P., and W. Grassi. 2011. Effects of external electric field on pool boiling: Comparison of terrestrial and microgravity data in the ARIEL experiment. Experimental Thermal and Fluid Science 35 (5): 780-7.

[8] Liu, F. -C, S. -W Chen, J. -R Wang, W. -K Lin, C. Shih, J. -D Lee, and J. -J Peir. 2015. "Experiment of Pool Subcooled Heat Transfer with and without Ultrasonic Vibration.".

[9] Arima, H., M. Monde, and Y. Mitsutake. 2003. "Heat Transfer in Pool Boiling of ammonia/water Mixture." Heat and Mass Transfer 39 (7): 535-543. doi:10.1007/s00231-002-0302-2.

[10] Gorenflo, D., U. Chandra, S. Kotthoff, and A. Luke. 2004. "Influence of Thermophysical Properties on Pool Boiling Heat Transfer of Refrigerants." International Journal of Refrigeration 27 (5): 492-502. doi:10.1016/j.ijrefrig.2004.03.004.

[11] Jensen, M. K. and D. L. Jackman. 1984. "PREDICTION OF NUCLEATE POOL BOILING HEAT TRANSFER COEFFICIENTS OF REFRIGERANT-OIL MIXTURES." Journal of Heat Transfer 106 (1): 184-190.

[12] Nishikawa, K., Fujita, Y., Ohta, H., and Hidaka, S., 1982, ‘‘Effects of System Pressure and Surface Roughness on Nucleate Boiling Heat Transfer,’’ Memoirs of the Faculty of Engineering, Kyushu University, 42(2), pp. 95–111.

[13] H.D. Kim, J. Kim, M.H. Kim, Experimental studies on CHF characteristics of nano-fluids at pool boiling, Int. J. Multiph. Flow. 33 (2007) 691e706.

[14] S. Kim, H.D. Kim, H. Kim, H.S. Ahn, H. Jo, J. Kim, M.H. Kim, Effects of nano-fluid and surfaces with nano structure on the increase of CHF, Exp. Therm. Fluid Sci. 34 (2010) 87e495.

[15] M. Kole, T.K. Dey, Investigations on the pool boiling heat transfer and critical heat flux of ZnO-ethylene glycol nanofluids, Appl. Therm. Eng. 37 (2012)112e119.

[16] S. Soltani, S.G. Etemad, J. Thibault, Pool boiling heat transfer of non-Newtonian nanofluids, Int. Commun. Heat. Mass Transf. 37 (2010) 29e33.

[17] Chopkar, M., A. K. Das, I. Manna, and P. K. Das. 2008. "Pool Boiling Heat Transfer Characteristics of ZrO2-Water Nanofluids from a Flat Surface in a Pool." Heat and Mass Transfer/Waerme- Und Stoffuebertragung 44 (8): 999-1004. doi:10.1007/s00231-007-0345-5.

[18] Das, S. K., G. Prakash Narayan, and A. K. Baby. 2008. "Survey on Nucleate Pool Boiling of Nanofluids: The Effect of Particle Size Relative to Roughness." Journal of Nanoparticle Research 10 (7): 1099-1108. doi:10.1007/s11051-007-9348-x.

[19] S. Zeinali Heris, F. Mohammadpur, A. Shakouri, Effect of electric field on thermal performance of thermosyphon heat pipes using nanofluids, Mater. Res. Bull. 53 (2014) 21e27.

[20] Kim, H., H. S. Ahn, and M. H. Kim. 2010. "On the Mechanism of Pool Boiling Critical Heat Flux Enhancement in Nanofluids."

[21] Golubovic, M. N., H. D. Madhawa Hettiarachchi, W. M. Worek, and W. J. Minkowycz. 2009. "Nanofluids and Critical Heat Flux, Experimental and Analytical Study." Applied Thermal Engineering 29 (7): 1281-1288. doi:10.1016/j.applthermaleng.2008.05.005.

[22] Amiri, A., M. Shanbedi, H. Amiri, S. Z. Heris, S. N. Kazi, B. T. Chew, and H. Eshghi. 2014. "Pool Boiling Heat Transfer of CNT/water Nanofluids." Applied Thermal Engineering 71 (1): 450-459.

[23] Kathiravan, R., R. Kumar, A. Gupta, R. Chandra, and P. K. Jain. 2011. "Pool Boiling Characteristics of Multiwalled Carbon Nanotube (CNT) Based Nanofluids Over a Flat Plate Heater." International Journal of Heat and Mass Transfer 54 (5-6): 1289-1296.

[24] Jones, B. J., J. P. McHale, and S. V. Garimella. 2009. "The Influence of Surface Roughness on Nucleate Pool Boiling Heat Transfer." Journal of Heat Transfer 131 (12): 1-14.

[25] Kang, M. -G. 2000. "Effect of Surface Roughness on Pool Boiling Heat Transfer." International Journal of Heat and Mass Transfer 43 (22): 4073-4085.

[26] McHale, J. P. and S. V. Garimella. 2010. "Bubble Nucleation Characteristics in Pool Boiling of a Wetting Liquid on Smooth and Rough Surfaces." International Journal of Multiphase Flow 36 (4): 249-260.

[27] Honda, H., H. Takamatsu, and J. J. Wei. 2002. "Enhanced Boiling of FC-72 on Silicon Chips with Micro-Pin-Fins and Submicron-Scale Roughness." Journal of Heat Transfer 124 (2): 383-390.

[28] Launay, S., A. G. Fedorov, Y. Joshi, A. Cao, and P. M. Ajayan. 2006. "Hybrid Micro-Nano Structured Thermal Interfaces for Pool Boiling Heat Transfer Enhancement." Microelectronics Journal 37 (11): 1158-1164. doi:10.1016/j.mejo.2005.07.016.

[29] Nimkar, N. D., S. H. Bhavnani, and R. C. Jaeger. 2006. "Effect of Nucleation Site Spacing on the Pool Boiling Characteristics of a Structured Surface." International Journal of Heat and Mass Transfer 49 (17-18): 2829-2839.

[30] Ramaswamy, C., Y. Joshi, W. Nakayama, and W. B. Johnson. 2002. "High-Speed Visualization of Boiling from an Enhanced Structure."

[31] Zou, A. and S. C. Maroo. 2013. "Critical Height of micro/nano Structures for Pool Boiling Heat Transfer Enhancement." Applied Physics Letters 103 (22). doi:10.1063/1.4833543

[32] Wei, J. J., L. J. Guo, and H. Honda. 2005. "Experimental Study of Boiling Phenomena and Heat Transfer Performances of FC-72 Over Micro-Pin-Finned Silicon Chips." Heat and Mass Transfer/Waerme- Und Stoffuebertragung 41 (8): 744-755.

[33] Yu, C. K. and D. C. Lu. 2007. "Pool Boiling Heat Transfer on Horizontal Rectangular Fin Array in Saturated FC-72." International Journal of Heat and Mass Transfer 50 (17-18): 3624-3637.

[34] Cooke, D. and S. G. Kandlikar. 2012. "Effect of Open Microchannel Geometry on Pool Boiling Enhancement." International Journal of Heat and Mass Transfer 55 (4): 1004-1013.

[35] Han, K., Enright, R., and Wang, E.N., 2012, “Structured surface for enhanced pool boiling heat transfer,” Applied Physics Letters, vol. 100, pp. 241603.

[36] Tang, Y., Tang, B., Li, Q., Qing, J., Lu, L., and Chen, K., 2012, “Pool-boiling enhancement by novel metallic nanoporous surface,” Experimental Thermal and Fluid Science vol. 44, pp. 197-198.

[37] Byon, C., Choi, S., and Kim, S.J., 2013, “Critical heat flux of bi-porous sintered copper coating in FC-72,” International Journal of Heat and Mass Transfer, vol. 65, pp. 655-661.

[38] Dong, L., X. Quan, and P. Cheng. 2014. "An Experimental Investigation of Enhanced Pool Boiling Heat Transfer from Surfaces with micro/nano-Structures." International Journal of Heat and Mass Transfer 71: 189-196.

[39] Zou, A. and S. C. Maroo. 2013. "Critical Height of micro/nano Structures for Pool Boiling Heat Transfer Enhancement." Applied Physics Letters 103 (22).

[40] Rahman, M. M., E. Ölçeroglu, and M. McCarthy. 2014. "Role of Wickability on the Critical Heat Flux of Structured Superhydrophilic Surfaces." Langmuir 30 (37): 11225-11234.

[41] Feng, B., K. Weaver, and G. P. Peterson. 2012. "Enhancement of Critical Heat Flux in Pool Boiling using Atomic Layer Deposition of Alumina." Applied Physics Letters 100 (5).

[42] Takata, Y., S. Hidaka, J. M. Cao, T. Nakamura, H. Yamamoto, M. Masuda, and T. Ito. 2005. "Effect of Surface Wettability on Boiling and Evaporation." Energy 30 (2-4 SPEC. ISS.): 209-220. doi:10.1016/j.energy.

[43] Takata, Y., S. Hidaka, M. Masuda, and T. Ito. 2003. "Pool Boiling on a Superhydrophilic Surface." International Journal of Energy Research 27 (2): 111-119. doi:10.1002/er.861

[44] Bourdon, B., P. Di Marco, R. Rioboo, M. Marengo, and J. De Coninck. 2013. "Enhancing the Onset of Pool Boiling by Wettability Modification on Nanometrically Smooth Surfaces." International Communications in Heat and Mass Transfer 45: 11-15.

[45] Hsu, C. -C and P. -H Chen. 2012. "Surface Wettability Effects on Critical Heat Flux of Boiling Heat Transfer using Nanoparticle Coatings." International Journal of Heat and Mass Transfer 55 (13-14): 3713-3719.

[46] Betz, A. R., J. Xu, H. Qiu, and D. Attinger. 2010. "Do Surfaces with Mixed Hydrophilic and Hydrophobic Areas Enhance Pool Boiling?" Applied Physics Letters 97 (14).

[47] Jo, H., H. S. Ahn, S. Kang, and M. H. Kim. 2011. "A Study of Nucleate Boiling Heat Transfer on Hydrophilic, Hydrophobic and Heterogeneous Wetting Surfaces." International Journal of Heat and Mass Transfer 54 (25-26): 5643-5652.

[48] Dhir, V. K. 2006. "Mechanistic Prediction of Nucleate Boiling Heat Transfer-Achievable Or a Hopeless Task?" Journal of Heat Transfer 128 (1): 1-12. doi:10.1115/1.2136366.

[49] Forster, K., and R. Greif. "HEAT TRANSFER TO A BOILING LIQUID MECHANISM AND CORRELATIONS. Progress Report No. 7 (58-40)." 1958.

[50] Zuber, Novak. "On the Correlation of Data in Nucleate Pool Boiling from a Horizontal Surface." *AIChE Journal* 3, no. 3 (1957): 9S-11S.

[51] Paul Laca, R. A. Wirtz, "Sub-atmospheric pressure pool boiling of water on a screen laminate-enhanced extended surface", Semiconductor Thermal Measurement and Management Symposium 2009. SEMI-THERM 2009. 25th Annual IEEE, pp. 9-16, 2009, ISSN 1065-2221.

[52] Gwang Hyeok Seo, Gyoodong Jeun, Sung Joong Kim, Pool boiling heat transfer characteristics of zircaloy and SiC claddings in deionized water at low pressure,

Experimental Thermal and Fluid Science, Volume 64, June 2015, Pages 42-53, ISSN 0894-1777,

[53] Florine Giraud, Romuald Rullière, Cyril Toublanc, Marc Clausse, Jocelyn Bonjour, Subatmospheric pressure boiling on a single nucleation site in narrow vertical spaces, International Journal of Heat and Fluid Flow, Volume 58, April 2016, Pages 1-10, ISSN 0142-727X,

[54] McGillis, W.R., and Carey, V.P., 1991, “Pool Boiling Enhancement Techniques for Water at Low Pressure,” Seventh IEEE SEMI-THERMTM Symposium, pp. 64-72.

[55] Das, A.K., Das, P.K., and Saha, P., 2009, “Performance of Different Structured Surfaces in Nucleate Pool Boiling,” Applied Thermal Engineering, vol. 29, pp. 3643-3653.

[56] Derby, M. M., Chatterjee, A., Peles, Y., & Jensen, M. K.(2014). Flow condensation heat transfer enhancement in a mini-channel with hydrophobic and hydrophilic patterns. International Journal of Heat and Mass Transfer, 68, 151-160.

[57] Geim, A. K. and K. S. Novoselov. 2007. "The Rise of Graphene." Nature Materials 6 (3): 183-191.

[58] Park, S. -S, Y. H. Kim, Y. H. Jeon, M. T. Hyun, and N. -J Kim. 2015. "Effects of Spray-Deposited Oxidized Multi-Wall Carbon Nanotubes and Graphene on Pool-Boiling Critical Heat Flux Enhancement." Journal of Industrial and Engineering Chemistry 24: 276-283.

[59] Ahn, H. S., J. M. Kim, T. Kim, S. C. Park, J. M. Kim, Y. Park, D. I. Yu, et al. 2014. "Enhanced Heat Transfer is Dependent on Thickness of Graphene Films: The Heat Dissipation during Boiling." Scientific Reports 4.

[60] Ahn, H. S., J. M. Kim, J. M. Kim, S. C. Park, K. Hwang, H. J. Jo, T. Kim, D. W. Jerng, M. Kaviany, and M. H. Kim. 2015. "Boiling Characteristics on the Reduced Graphene Oxide Films." Experimental Thermal and Fluid Science 60: 361-366.

[61] Kim, J. M., T. Kim, J. Kim, M. H. Kim, and H. S. Ahn. 2014. "Effect of a Graphene Oxide Coating Layer on Critical Heat Flux Enhancement Under Pool Boiling." International Journal of Heat and Mass Transfer 77: 919-927.

[62] Seo, H., J. H. Chu, S. -Y Kwon, and I. C. Bang. 2015. "Pool Boiling CHF of Reduced Graphene Oxide, Graphene, and SiC-Coated Surfaces Under Highly Wettable FC-72." International Journal of Heat and Mass Transfer 82: 490-502.

[63] Kousalya, A. S., A. Kumar, R. Paul, D. Zemlyanov, and T. S. Fisher. 2013. "Graphene: An Effective Oxidation Barrier Coating for Liquid and Two-Phase Cooling Systems." Corrosion Science 69: 5-10.

[64] Lee, S. W., K. M. Kim, and I. C. Bang. 2013. "Study on Flow Boiling Critical Heat Flux Enhancement of Graphene oxide/water Nanofluid." International Journal of Heat and Mass Transfer 65: 348-356.

[65] T. Bartels-Rausch, V. Bergeron, J. H. E. Cartwright, R. Escribano, J. L. Finney, H. Grothe, P. J. Gutiérrez, J. Haapala, W. F. Kuhs, J. B. C. Pettersson, S. D. Price, C. I. Sainz-Díaz, D. J. Stokes, G. Strazzulla, E. S. Thomson, H. Trinks and N. Uras-Aytemiz. Ice structures, patterns, and processes: A view across the icefields. Rev. Mod. Phys. 84(2), pp. 885-944. 2012. DOI: 10.1103/RevModPhys.84.885.

[66] A. Bonakdar, M. Rezaei, R. L. Brown, V. Fathipour, E. Dexheimer, S. J. Jang and H. Mohseni. Deep-UV microsphere projection lithography. Opt. Lett. 40(11), pp. 2537-2540. 2015. DOI: 10.1364/OL.40.002537.

[67] O. Shavdina, L. Berthod, T. Kämpfe, S. Reynaud, C. Veillas, I. Verrier, M. Langlet, F. Vocanson, P. Fugier, Y. Jourlin and O. Dellea. Large area fabrication of periodic TiO2 nanopillars using microsphere photolithography on a photopatternable sol-gel film. Langmuir 31(28), pp. 7877-7884. 2015. DOI: 10.1021/acs.langmuir.5b01191.

[68] A. Van Dyke, D. Collard, M. M. Derby and A. R. Betz, "Droplet Coalescence and Freezing on Hydrophilic, Hydrophobic, and Biphilic Surfaces," Appl.Phys.Lett., vol. 107, pp. 141602, 2015.

[69] R. N. Leach, F. Stevens, S. C. Langford and J. T. Dickinson. Dropwise condensation: Experiments and simulations of nucleation and growth of water drops in a cooling system. Langmuir 22(21), pp. 8864-8872. 2006. DOI: 10.1021/la061901+.

[70] S. Jung, M. K. Tiwari and D. Poulikakos. Frost halos from supercooled water droplets. Proc. Natl. Acad. Sci. U. S. A. 109(40), pp. 16073-16078. 2012. DOI: 10.1073/pnas.1206121109.

[71] S. Jung, M. K. Tiwari, N. V. Doan and D. Poulikakos. Mechanism of supercooled droplet freezing on surfaces. *Nat. Commun. 3*2012. DOI: 10.1038/ncomms1630.

[72] J. B. Boreyko, R. R. Hansen, K. R. Murphy, S. Nath, S. T. Retterer and C. P. Collier. Controlling condensation and frost growth with chemical micropatterns. *Sci. Rep. 6*2016. DOI: 10.1038/srep19131.

[73] D. Lamb and W. D. Scott. Linear growth rates of ice crystals grown from the vapor phase. J. Cryst. Growth 12(1), pp. 21-31. 1972. DOI: 10.1016/0022-0248(72)90333-8.